Geol. Mag. **154** (3), 2017, pp. 419–440. © Cambridge University Press 2016
doi:10.1017/S0016756816000042

Age and geochemistry of the Zhaheba ophiolite complex in eastern Junggar of the Central Asian Orogenic Belt (CAOB): implications for the accretion process of the Junggar terrane

XIAN-TAO YE*‡, CHUAN-LIN ZHANG‡†, HAI-BO ZOU§, CHUN-YAN YAO‡ & YONG-GUAN DONG‡

*Chinese Academy of Geological Sciences, Beijing, 100037, China
‡Nanjing Institute of Geology and Mineral Resources, Nanjing 210016, China
§Department of Geosciences, Auburn University, Auburn, 36849-5305, USA

(*Received* 18 August 2015; *accepted* 8 January 2016; *first published online* 18 April 2016)

Abstract – We report new field observations, zircon U–Pb ages and geochemical data for the discrete members of the Zhaheba ophiolite complex in northeastern Junggar of the Central Asian Orogenic Belt (CAOB) with the aim to understand the accretion process of the eastern Junggar terrane. The zircon age data reveal that the cumulates of the Zhaheba ophiolite crystallized at ~485 Ma while the volcanic sequences erupted at ~400 Ma. Thus, the volcanic sequences are not members of the Zhaheba ophiolite. Chromian spinels from the serpentinite have comparable elemental compositions to those of spinels from MORB-type ophiolites. Similarly, the rift affinity of clinopyroxene and positive zircon $\varepsilon_{Hf}(t)$ (13–20) and mantle $\delta^{18}O$ (+5.37‰) values of the cumulates imply that the cumulates crystallized from primitive magmas derived from a depleted mantle source. Elemental and Nd isotopic compositions indicate that the basalts in the Zhaheba area were derived from partial melting of a mantle wedge metasomatized by adakitic melts and/or subduction-related fluids. The data presented in this contribution, together with previous studies, indicate that the Zhaheba–Almantai and Kelameili ophiolites were MORB-type, which implies that there were at least two mid-ocean ridges during Ordovician to early Devonian times in the Junggar Ocean. In the earlier stage, intra-oceanic subduction led to the formation of the intra-oceanic arc, and then the Kelameili ophiolite accreted to an intra-oceanic accretionary wedge. In the later stage, the Zhaheba–Almantai ophiolite accreted to the accretionary wedge along the southern margin of the Iritish suture zone during the roll-back of the subduction zone from north to south.

Keywords: Zhaheba ophiolite, MORB-type, accretion process, Central Asian Orogenic Belt (CAOB), Junggar terrane .

1. Introduction

Ophiolites, as well as their dismembered equivalents, which generally occur along suture zones in both collisional-type and accretionary-type orogenic belts (e.g. Xiao *et al.* 2008; Lister & Forster, 2009; Yellappa *et al.* 2012; Santosh *et al.* 2012, 2013; Saccani *et al.* 2013), contain important information about partial melting of the oceanic mantle, the ocean–continent transformation process and the tectonic evolution of orogenies (Niu, 1997; Cawood *et al.* 2009; Xiao *et al.* 2009*a*). Classification of ophiolites has been one of the most important issues in ophiolite studies since the Penrose symposium on ophiolites (Coleman, 1977; Nicolas, 1989; Cloos, 1993; Lagabrielle *et al.* 2000; Dilek & Flower, 2003; Cawood *et al.* 2009; Pearce, 2014). In a recent synthesis, Dilek & Furnes (2011) classified ophiolites into six major groups: continental margin, mid-ocean ridge, plume, supra-subduction zone (SSZ), volcanic arc and accretionary. Using immobile element geochemistry, Pearce (2014) divided ophiolites into two main types, i.e. mid-ocean-ridge type and SSZ-ridge type. The mid-ocean ridge ophiolites can be subdivided into N-type, E-type and P-type ophiolites, while the SSZ-ridge type ophiolites include a subduction-initiation type, back-arc basin type and ridge-subduction type.

Various types of ophiolite complexes are widely distributed in the Central Asian Orogenic Belt (CAOB), the largest Phanerozoic accretionary orogen in the world (Şengör, Natalin & Burtman, 1993; Jahn, Wu & Chen, 2000; Windley *et al.* 2002; Xiao *et al.* 2004, 2009*a*) (Fig. 1a). The ages of these ophiolites range from Vendian to Mesozoic, indicating the long evolution history of the CAOB (Xiao *et al.* 2009*a*,*b*; Wilhem, Windley & Stampfli, 2012). In eastern Junggar, which is one of the most important sections of the CAOB, several ophiolites have been identified over the past dozen years, including, from south to north, the Kelameili, Zhaheba–Almantai, Qiaoxiahala and Kuerti ophiolites (Xinjiang BGMR, 1993; Zhang *et al.* 2003; Jian *et al.* 2003; Xiao *et al.* 2009*a*) (Fig. 1b). Though many studies have been carried out on these ophiolites, their detailed rock associations, geochronology, geochemistry

†Author for correspondence: zchuanlin1968@gmail.com

https://doi.org/10.1017/S0016756816000042 Published online by Cambridge University Press

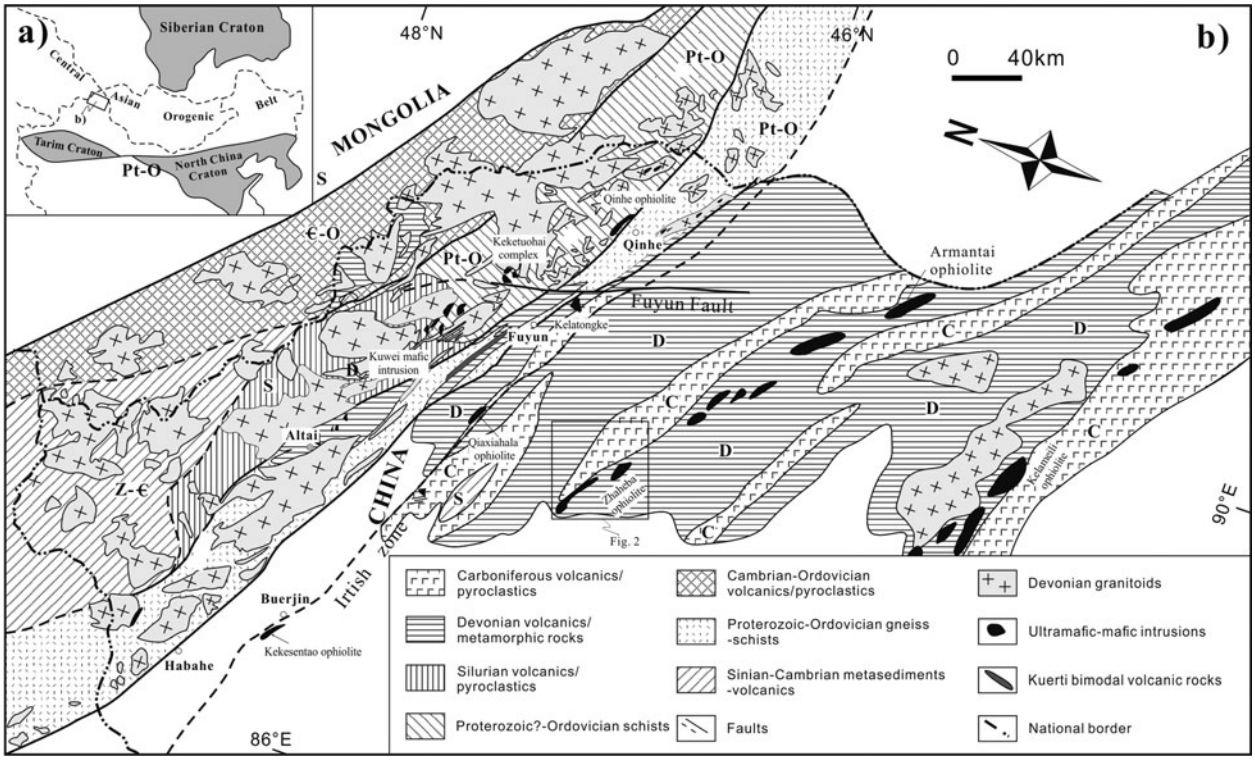

Figure 1. (a) Schematic geological map of the Central Asian Orogenic Belt (CAOB); (b) generalized geological map of the Chinese eastern Junggar and Altai orogen showing the distribution of ophiolites in eastern Junggar and along the Iritish suture zone (modified after Wang *et al.* 2009).

and tectonic incorporation processes are still poorly known. In this contribution, we report detailed field observations, petrography, ages and geochemistry of the Zhaheba ophiolite complex on the northern margin of the Junggar terrane in order to (1) better understand the accretion of individual members of the eastern Junggar terrane and (2) decipher the incorporation process of diverse-type rocks in an ophiolite mélange.

2. Regional geology, field observations and petrography

The Zhaheba ophiolite complex represents the northwestern section of the Zhaheba–Almantai ophiolite belt, which is distributed along the southern margin of the Erqis suture zone in a NW direction (Figs 1b, 2). The main rocks include serpentinite, cumulate, basaltic–andesitic lava and minor tuff and carbonate. The cumulate includes gabbro and minor pegmatitic gabbro, and occurs as small stocks or dykes distributed over several tens to hundreds of square metres. The cumulate intruded serpentinite but no chilled margin has been observed (Fig. 3a). Field observations identified at least 15 cumulate stocks and dykes. The serpentinite crops out in the southwest and is structurally mingled into the lower member of the Devonian basaltic–andesitic sedimentary sequence (Fig. 2, see following descriptions). Occasionally basalt stripes 1–5 m in length and less than 1 m in width can be seen in the serpentinite. Obviously these basalt stripes were structurally mixed into the serpentinite. The serpentinite composes > 90 % serpentine, with minor magnetite and spinel (Fig. 3b, c). Magnetite generally occurs in the fissures of the serpentine and is the by-product of sepentinization of dunite or harzburgite (e.g. Zhang *et al.* 2013). No relict olivine or orthopyroxene was observed in thin-sections. The gabbro mainly comprises plagioclase (40–70 %) and clinopyroxene (30–50 %) as well as minor orthopyroxene (5–10 %) and occasional olivine (Fig. 3d). Accessory minerals include Fe–Ti oxides and zircon. These cumulates show a massive structure and are medium grained to coarse grained without significant deformation or hydrothermal alteration, with the exception of slight sericitization of plagioclase and serpentinization of pyroxene in several thin-sections. The basaltic–andesitic volcanic sedimentary sequence was locally divided into the lower to middle Devonian Tuorangekuduke Formation (TF) and Wendukala Formation (WF) and the upper Devonian Jianggesayi Formation (JF) (Yuan *et al.* 2006). To the northeast of the Devonian sequences are Carboniferous volcaniclastic sedimentary strata in fault contact with the Devonian strata. The TF was divided into three members according to their rock associations, which include tuff and crystal tuff, volcaniclastic rocks and tuff-bearing sandstones (Fig. 2). In the lower member, a small carbonate lens conformably overlying basaltic–andesitic lava was observed, sharing the typical structural features of a seamount. This basaltic–andesitic lava in the TF had been recognized as a member of the Zhaheba ophiolite because of their close spatial relationship (Xinjiang BGMR, 1993). Both the Devonian

https://doi.org/10.1017/S0016756816000042 Published online by Cambridge University Press

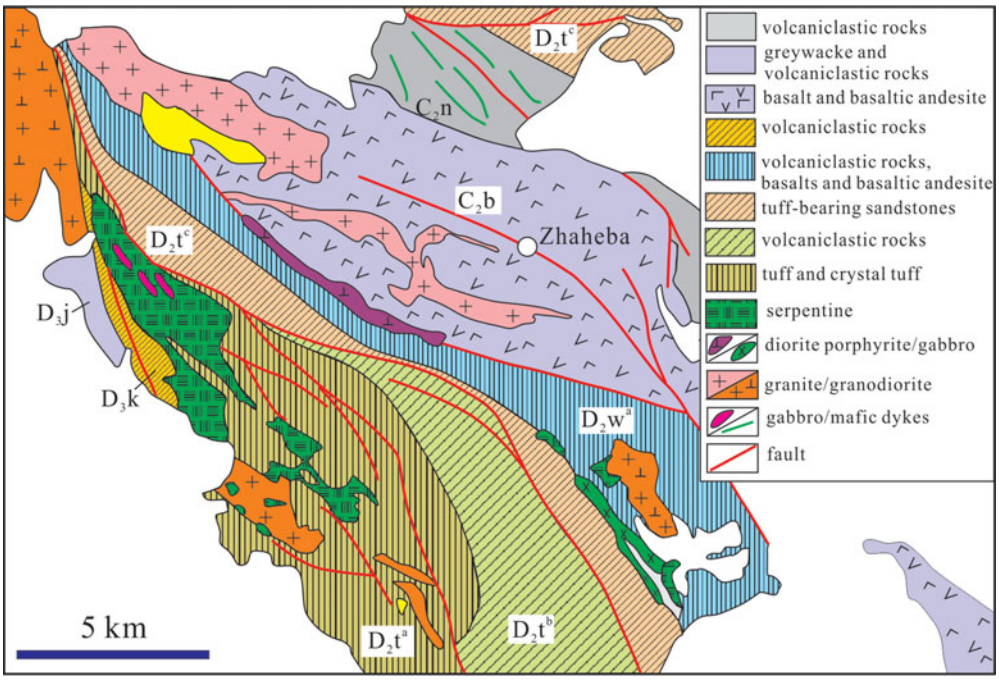

Figure 2. (Colour online) Geological map of the Zhaheba ophiolite complex (modified after Niu *et al.* 2007, 2009*a* and Xinjiang BGMR, 1993).

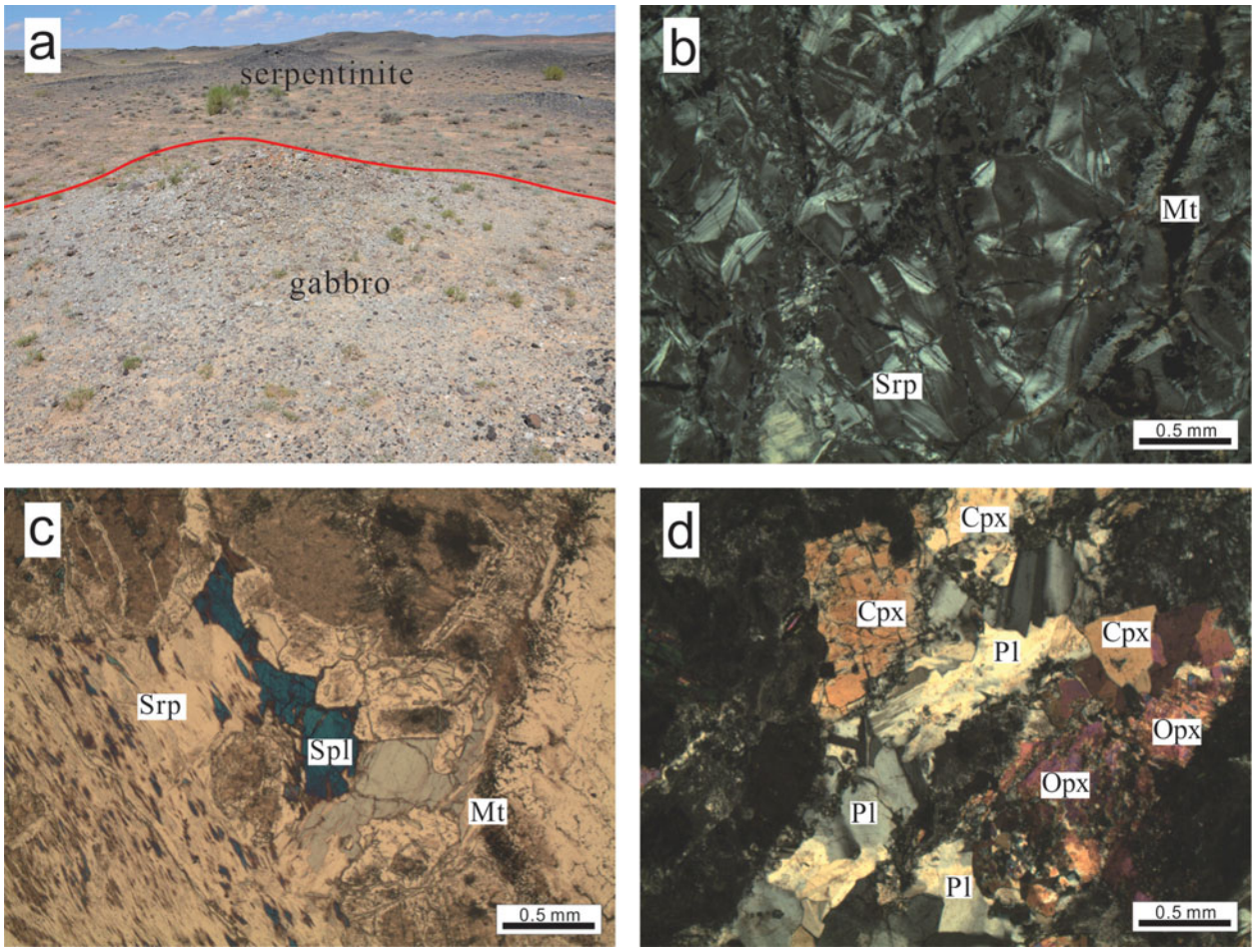

Figure 3. (Colour online) Field photographs and microscopic photographs of different members from the Zhaheba ophiolite. (a) Cumulate intruded serpentinite without chilled margin. (b, c) The serpentinite comprises > 90 % serpentine and minor magnetite and spinel. (d) The gabbro is mainly composed of plagioclase, clinopyroxene and minor orthopyroxene. Cpx – clinopyroxene; Mt – magnetite; Opx – orthopyroxene; Pl – plagioclase; Spl – spinel; Srp – serpentine.

https://doi.org/10.1017/S0016756816000042 Published online by Cambridge University Press

and Carboniferous volcanic sedimentary strata are intensively foliated or show schistose texture.

3. Analytical procedures

3.a. Zircon U–Pb dating and Hf–O isotope analysis

Zircons were separated from a gabbro sample (2013ALT01, 46° 32′ 51“ N, 89° 2′ 49” E) and a tuff sample (2013ALT02, 46° 33′ 2“ N, 89° 2′ 36” E) collected from the tuff layer in the lower member of the TF. Zircon separation was carried out using conventional magnetic and density techniques. Zircon grains were then hand-picked under a binocular microscope. Zircon grains and zircon reference standards were mounted in epoxy mounts, which were then polished to section the crystals for analysis. All zircons were documented with transmitted and reflected light micrographs as well as cathodoluminescence (CL) images to reveal their internal structures. Zircon ages and Hf isotope compositions were analysed using the laser ablation inductively coupled plasma mass spectrometry (LA-ICP-MS) method at the Tianjin Institute of Geology and Mineral Resources, Chinese Geological Survey. The detailed analytical procedures have been documented in Geng *et al.* (2011). Hf isotopes were analysed in the same spot as used for the U–Pb analyses. Data reduction was performed off-line by ICP-MS Data Cal (Liu *et al.* 2010) and Isoplot (Ludwig, 2003). The weighted mean ages are quoted at the 95 % confidence level. Zircon U–Pb age data and Hf isotope compositions are listed in online Supplementary Material Table S1 and online Supplementary Material Table S2, respectively, available at http://journals.cambridge.org/geo.

Zircon oxygen isotopes were measured using the Cameca IMS 1280 SIMS at the Institute of Geology and Geophysics, Chinese Academy of Sciences in Beijing, with analytical procedures similar to those reported by Li *et al.* (2010*a*). Measured $^{18}O/^{16}O$ ratios were normalized by using Vienna Standard Mean Ocean Water compositions (VSMOW, $^{18}O/^{16}O = 0.0020052$), and then corrected for the instrumental mass fractionation factor (IMF) using Penglai zircons as a reference standard with a $\delta^{18}O$ value of 5.31 ‰ (Li *et al.* 2010*b*). Ten measurements of the Qinghu zircon standard during the course of this study yield a weighted mean $\delta^{18}O$ of 5.44 ± 0.21 ‰ (2SD), which is consistent within errors with the reported value of 5.4 ± 0.2 ‰ (Li *et al.* 2013). Zircon oxygen isotopic data are listed in online Supplementary Material Table S3 available at http://journals.cambridge.org/geo.

3.b. Mineral analysis

Mineral compositions were determined on polished thin-sections using an automated JEOL 8800 electron microprobe equipped with five wavelength spectrometers at the Guangzhou Institute of Geochemistry, Chinese Academy of Sciences. Operating conditions were 15 keV accelerating voltage and 15 nA beam current with 20 s counting time. Representative mineralogical data are listed in online Supplementary Material Tables S4 and S5 available at http://journals.cambridge.org/geo.

3.c. Whole-rock analysis

Whole-rock major- and trace-element compositions were analysed at the Guangzhou Institute of Geochemistry, Chinese Academy of Sciences. Major elements were analysed using a Rigaku ZSX100e XRF following the analytical procedures described by Li *et al.* (2004). Analytical precision is generally better than 2 %. Trace elements were analysed using a Perkin-Elmer Sciex ELAN 6000 ICP-MS following procedures described by Li *et al.* (2004). Roughly 50 mg sample powders from each sample were dissolved in high-pressure Teflon bombs using a $HF + HNO_3$ mixture. An internal standard solution containing single element Rh was used to monitor signal drift during ion counting. The USGS standards BCR-1, W-2 and G-2, and the Chinese National standards GSR-1 and GSR-3, were used for calibrating element concentrations of measured samples. In-run analytical precision for most elements was better than 3–5 %. The analytical results are listed in Table 1.

Samples for Nd–Sr isotopic measurements were spiked and dissolved in Teflon bombs with $HF + HNO_3$ acid, and then separated by conventional cation-exchange techniques. The isotopic measurements were performed on a Micromass Isoprobe multi-collector inductively coupled plasma mass spectrometer (MC-ICP-MS) at the State Key Laboratory of Ore Deposit Geochemistry, Institute of Geochemistry, Chinese Academy of Sciences. The detailed procedure has been described by Li *et al.* (2004). The measured $^{87}Sr/^{86}Sr$ and $^{143}Nd/^{144}Nd$ ratios are corrected to $^{86}Sr/^{88}Sr = 0.1194$ and $^{146}Nd/^{144}Nd = 0.7219$, respectively. The measured $^{87}Sr/^{86}Sr$ average ratios were 0.710288 for the NBS987 standard and 0.705069 for BCR-1, and the $^{143}Nd/^{144}Nd$ average ratios were 0.512104 for JNdi-1 and 0.512671 for BCR-1. The analytical results and calculated parameters are listed in Table 2.

4. Analytical results

4.a. Zircon U–Pb ages

Zircons from the gabbro sample are translucent and colourless. Most grains are short prismatic with lengths ranging from 100 to 150 μm and aspect ratios ranging from 1:1 to 2:1. In CL images, the zircons display wide oscillatory zoning, features characteristic of zircons in mafic magmatic rocks (see inset of Fig. 4a). Thirty analyses were conducted on this sample, and the results show variable U (22–123 ppm) and Th (8–57 ppm) contents with Th/U ratios ranging from 0.4 to 0.8. Twenty-seven analyses on 30 zircons yielded consistent results with a concordant age within analytical error and a weighted mean age of 485.8 ± 2.5 Ma

https://doi.org/10.1017/S0016756816000042 Published online by Cambridge University Press

Table 1. Geochemical compositions of the serpentinite, cumulate and basalts from the Zhaheba ophiolite complex

Sample Rock type	2013ALT01-1 SP	2013ALT01-3 G	20132ALT01-4 SP	2013ALT01-5 SP	2013ALT01-6 SP	2013ALT01-7 SP	2013ALT01-8 SP	2013ALT01H1 G	2013ALT01H2 G	2013ALT01H4 G
					Major elements (%)					
SiO_2	38.70	48.20	39.41	38.62	39.22	39.82	39.05	47.22	46.48	51.27
TiO_2	0.05	0.20	0.05	0.05	0.04	0.05	0.04	0.14	0.12	0.27
Al_2O_3	0.61	1.96	1.04	0.67	0.90	0.74	0.90	18.28	19.64	19.33
Fe_2O_3	8.44	4.68	7.87	9.36	7.57	7.16	7.84	3.67	3.24	3.89
MnO	0.08	0.10	0.11	0.11	0.11	0.09	0.11	0.08	0.07	0.08
MgO	38.21	24.59	38.82	37.89	39.09	39.31	38.44	10.04	9.03	5.89
CaO	0.12	15.42	0.15	0.14	0.29	0.10	0.14	13.11	13.56	9.54
Na_2O	0.40	0.17	0.29	0.59	0.23	0.04	0.92	2.91	3.19	5.85
K_2O	0.03	0.02	0.03	0.04	0.03	0.03	0.06	0.46	0.24	0.12
P_2O_5	0.00	0.01	0.00	0.01	0.00	0.01	0.02	0.01	0.00	0.02
LOI	12.19	4.46	12.27	12.26	12.36	12.83	12.54	3.82	4.20	3.44
TOT	98.84	99.81	100.04	99.72	99.84	100.19	100.05	99.72	99.78	99.71
Alk	0.43	0.19	0.32	0.63	0.26	0.07	0.98	3.36	3.43	5.98
Mg no.	90	91	91	89	91	92	91	84	85	75
					Trace elements (ppm)					
Li	0.012	0.073	0.100	/	/	0.220	0.172	36.7	44.3	7.44
Be	5.56	47.4	6.96	6.52	10.7	6.41	6.39	0.000	/	0.442
Sc	29.3	115	32.5	28.6	45.1	28.5	23.2	20.1	22.1	19.4
V	1590	1820	1470	1340	1950	1660	1330	91.2	77.4	76.9
Cr	99.3	58.8	97.2	98.2	97.0	103	93.2	217	169	23.3
Co	1960	711	2050	1930	1930	2070	1940	27.2	24.3	20.1
Ni	7.89	3.86	7.07	5.82	6.79	5.36	4.83	212	200	79.3
Cu	37.2	26.9	52.5	45.1	47.1	45.7	58	43.82	40.72	34.44
Zn	1.13	2.60	1.42	1.36	1.30	1.42	1.17	22.2	27.6	35.8
Ga	0.012	0.073	0.100	/	/	0.220	0.172	10.1	10.4	15.2
Rb	0.134	0.076	0.079	0.061	0.052	0.066	0.053	2.21	1.16	0.50
Sr	18.8	50.2	7.95	6.31	8.74	8.60	8.01	395	420	405
Y	0.251	4.67	0.349	0.250	0.527	0.225	0.202	3.42	2.69	13.2
Zr	0.425	5.20	2.33	1.68	0.609	1.17	0.612	4.45	2.67	39.1
Nb	0.168	0.111	0.090	0.085	0.240	0.105	0.052	0.132	0.094	0.922
Cd	0.011	0.040	0.020	0.016	0.007	0.004	0.005	0.017	0.021	0.031
Sn	0.228	0.629	0.234	0.118	0.101	0.109	0.008	0.206	0.114	1.55
Cs	0.027	0.008	0.014	0.010	0.005	0.007	0.007	0.497	0.622	0.765
Ba	66.8	8.93	56.2	29.5	2.43	65.3	19.7	95.5	94.4	49.8
La	0.053	1.260	0.188	0.105	0.506	0.136	0.044	0.546	0.478	5.650
Ce	0.104	4.920	0.358	0.220	1.930	0.286	0.088	1.280	1.090	13.600
Pr	0.011	0.895	0.032	0.022	0.127	0.030	0.013	0.201	0.171	1.870
Nd	0.046	5.090	0.097	0.063	0.493	0.103	0.057	1.030	0.842	8.650
Sm	0.015	1.310	0.009	0.010	0.094	0.018	0.007	0.347	0.291	1.940
Eu	/	0.473	0.005	0.006	0.024	0.003	0.003	0.265	0.259	0.904
Gd	0.021	1.267	0.028	0.027	0.067	0.019	0.014	0.520	0.441	1.975
Tb	0.004	0.175	0.007	0.004	0.012	0.002	0.003	0.084	0.068	0.343
Dy	0.033	0.908	0.042	0.028	0.079	0.029	0.016	0.538	0.450	2.090
Ho	0.007	0.180	0.012	0.009	0.021	0.008	0.006	0.116	0.094	0.457
Er	0.021	0.467	0.040	0.026	0.073	0.019	0.018	0.353	0.289	1.390

https://doi.org/10.1017/S0016756816000042 Published online by Cambridge University Press

Table 1. Continued

Sample Rock type	2013ALT01-1 SP	2013ALT01-3 G	20132ALT01-4 SP	2013ALT01-5 SP	2013ALT01-6 SP	2013ALT01-7 SP	2013ALT01-8 SP	2013ALT01H1 G	2013ALT01H2 G	2013ALT01H4 G
Tm	0.005	0.064	0.008	0.005	0.009	0.003	0.003	0.051	0.044	0.222
Yb	0.021	0.347	0.044	0.042	0.072	0.031	0.033	0.310	0.257	1.450
Lu	0.004	0.047	0.007	0.008	0.011	0.005	0.005	0.049	0.043	0.219
Hf	0.011	0.232	0.036	0.044	0.012	0.034	0.008	0.123	0.090	0.993
Ta	0.090	0.036	0.038	0.037	0.068	0.026	0.025	0.046	0.031	0.067
W	0.268	1.710	6.600	1.880	0.993	0.233	1.150	1.570	0.516	0.195
Pb	0.406	0.092	0.127	0.112	0.099	0.199	0.054	0.168	0.191	0.695
Th	0.046	0.034	0.014	0.028	0.050	0.030	0.010	0.050	0.029	0.130
U	0.191	0.144	0.203	0.364	0.042	0.094	0.079	0.066	0.042	0.073
sample Rock type	2013ALT01H5 G	2013ALT01H6 G	2013ALT01H7 B (G1)	2013ALT01H8 BA (G1)	2013ALT01H9 B (G1)	2013ALT03H2 B (G1)	2013ALT03H3 B (G1)	2013ALT03H4 B (G1)	2013ALT03H5 B (G1)	2013ALT01H3 B (G2)
					Major elements (%)					
SiO_2	49.17	45.87	48.79	53.19	51.91	50.40	50.54	50.52	51.22	52.37
TiO2	0.34	0.15	1.40	1.24	1.31	1.70	1.63	1.31	1.17	0.33
Al_2O_3	18.99	19.58	16.59	16.19	15.93	15.87	16.76	15.55	15.48	19.61
Fe_2O_3	4.52	3.34	7.88	7.11	7.43	9.09	9.50	9.42	7.82	3.44
MnO	0.09	0.08	0.11	0.10	0.11	0.13	0.11	0.14	0.12	0.07
MgO	6.87	7.42	4.80	4.28	4.41	5.89	3.29	6.06	7.14	4.88
CaO	11.03	12.61	6.22	5.75	6.39	6.75	4.52	7.49	8.26	8.90
Na_2O	4.86	7.38	8.72	8.39	8.00	4.52	7.31	4.80	4.08	7.11
K_2O	0.13	0.11	0.39	0.31	0.42	2.04	0.33	1.27	2.03	0.17
P2O5	0.04	0.02	0.62	0.62	0.65	0.74	0.69	0.47	0.44	0.04
LOI	3.72	3.26	4.24	2.54	2.93	2.27	5.14	2.65	1.93	2.79
TOT	99.75	99.82	99.76	99.70	99.49	99.40	99.81	99.67	99.68	99.71
Alk	4.98	7.49	9.11	8.70	8.42	6.56	7.64	6.07	6.11	7.29
Mg#	75	81	55	54	54	56	41	56	64	74
					Trace elements (ppm)					
Li	9.09	4.95	1.16	1.12	1.47	9.08	40.4	5.29	6.82	5.71
Be	0.229	0.135	1.284	1.683	1.316	1.953	1.034	1.100	0.575	0.629
Sc	25.0	23.8	18.6	17.5	17.5	7.5	19.2	25.2	18.9	17.0
V	118	83.7	186	166	172	227	229	254	187	75.7
Cr	34.7	163	60.5	62.6	64.1	116	18.9	90.7	203	23.7
Co	24.2	21.6	26.9	23.6	24.6	27.8	28.5	28.0	28.0	16.4
Ni	94.7	175	63.6	50.7	51.4	76.8	27.7	57.3	132	71.1
Cu	52.94	55.59	92.06	61.97	42.93	79.94	12.75	113.3	74.27	18.41
Zn	44	24.6	101	92.4	99.8	148	129	93.5	78.6	30.4
Ga	14.5	10.9	11.1	13.1	11.9	18.0	21.2	18.4	16.2	16.2
Rb	0.547	0.413	6.240	2.340	3.790	2.870	8.060	9.650	12.900	0.357
Sr	395	817	1110	1290	1470	1320	516	1480	1360	392
Y	10.7	4.19	13.6	13.3	13.3	8.30	15.6	16.2	13.1	17.0
Zr	29.1	7.26	172	183	180	132	174	121	141	58.4
Nb	0.797	0.148	21.456	20.702	20.702	38.974	23.636	11.315	16.511	1.039
Cd	0.030	0.022	0.038	0.041	0.047	0.067	0.028	0.072	0.031	0.038
Sn	0.521	0.149	0.929	0.868	0.899	1.170	1.040	0.847	0.876	0.561
Cs	0.655	1.090	0.668	0.200	0.218	0.592	1.020	0.666	0.200	0.573
Ba	38.9	74.3	398	351	514	877	258	464	622	62.7

https://doi.org/10.1017/S0016756816000042 Published online by Cambridge University Press

Table 1. Continued

sample	2013ALT01H5	2013ALT01H6	2013ALT01H7	2013ALT01H8	2013ALT01H9	2013ALT03H2	2013ALT03H3	2013ALT03H4	2013ALT03H5	2013ALT01H3
Rock type	G	G	B (G1)	BA (G1)	B (G1)	B (G1)	B (G1)	B (G1)	B (G1)	B (G2)
La	3.97	1.20	39.60	46.70	47.30	23.40	43.00	25.20	32.90	6.56
Ce	9.78	2.67	79.50	89.10	89.80	61.30	83.80	51.70	65.30	16.30
Pr	1.390	0.354	9.130	9.920	10.100	6.910	9.620	6.070	7.380	2.320
Nd	6.400	1.730	35.60	37.70	38.50	28.60	36.90	24.50	28.60	10.800
Sm	1.530	0.490	5.690	5.750	6.150	4.950	5.970	4.550	4.710	2.490
Eu	0.789	0.350	1.747	1.797	1.909	1.465	1.820	1.495	1.419	1.040
Gd	1.665	0.668	4.207	4.414	4.244	3.791	4.382	3.846	3.589	2.758
Tb	0.277	0.111	0.562	0.613	0.601	0.511	0.593	0.540	0.477	0.446
Dy	1.750	0.676	2.650	2.630	2.730	2.380	2.860	2.800	2.290	2.710
Ho	0.375	0.140	0.502	0.483	0.497	0.429	0.538	0.542	0.404	0.594
Er	1.140	0.439	1.410	1.390	1.400	1.150	1.530	1.500	1.160	1.810
Tm	0.168	0.059	0.182	0.175	0.180	0.144	0.194	0.201	0.143	0.297
Yb	1.100	0.404	1.120	1.080	1.100	0.911	1.200	1.260	0.935	1.930
Lu	0.165	0.062	0.151	0.150	0.152	0.126	0.171	0.176	0.134	0.290
Hf	0.893	0.218	3.640	3.820	3.800	2.650	3.430	2.440	2.720	1.420
Ta	0.058	0.028	0.932	0.963	0.948	1.796	0.937	0.459	0.670	0.066
W	0.119	0.184	0.291	0.860	0.513	0.710	0.477	0.297	0.327	0.177
Pb	0.551	0.514	3.520	6.700	6.410	4.480	7.160	4.520	5.030	0.953
Th	0.175	0.091	3.790	4.420	4.410	0.575	3.370	2.340	3.300	0.123
U	0.064	0.057	1.050	1.160	1.180	0.557	1.360	0.850	0.935	0.084
sample	2013ALT01H11	2013ALT02H1	2013ALT02H2	2013ALT03H1	2013ALT03H6	2013ALT01H10	04Z06	04Z24	04Z29	03Z17
Rock type	B (G2)	B (G2)	B (G2)	B (G1)	B (G1)	B (G2)	BA (G1)	B (G1)	B (G1)	BA (G1)
					Major elements (%)					
SiO_2	49.68	47.09	47.56	45.89	53.28	43.15	55.38	50.24	50.85	57.65
TiO2	0.55	0.49	0.52	0.68	1.08	0.51	1.00	1.08	1.76	1.02
Al_2O_3	15.98	15.62	15.27	6.83	14.34	5.03	16.98	14.92	16.22	16.41
Fe_2O_3	7.00	7.59	7.81	10.30	9.88	14.76	7.02	8.41	9.95	9.06
MnO	0.12	0.14	0.14	0.19	0.13	0.21	0.11	0.11	0.12	0.12
MgO	7.40	8.07	8.04	11.70	3.13	27.83	4.68	7.21	5.50	2.82
CaO	11.08	11.76	11.17	15.48	5.15	4.22	5.16	7.96	6.06	3.41
Na_2O	4.37	4.61	4.81	3.60	6.76	0.28	6.64	4.19	4.38	5.55
K_2O	0.09	0.15	0.13	0.24	0.18	0.05	0.32	2.12	2.40	1.23
P2O5	0.09	0.11	0.11	0.04	0.38	0.04	0.41	0.51	0.82	0.34
LOI	3.36	4.13	3.98	4.96	5.71	3.63	1.68	3.30	1.78	2.36
TOT	99.70	99.75	99.55	99.90	100.00	99.74	99.38	100.05	99.84	99.97
Alk	4.45	4.76	4.94	3.84	6.93	0.33	6.96	6.31	6.78	6.78
Mg#	68	68	67	69	39	79	57	63	52	38

https://doi.org/10.1017/S0016756816000042 Published online by Cambridge University Press

Table 1. Continued

sample Rock type	2013ALT01H11 B (G2)	2013ALT02H1 B (G2)	2013ALT02H2 B (G2)	2013ALT03H1 B (G1)	2013ALT03H6 B (G1)	2013ALT01H10 B (G2)	04Z06 BA (G1)	04Z24 B (G1)	04Z29 B (G1)	03Z17 BA (G1)
				Trace elements (ppm)						
Li	19.4	36.9	42.4	26.0	32.4	17.9	/	/	/	/
Be	0.395	0.153	0.358	1.198	0.947	0.468	/	/	/	/
Sc	32.5	33.2	34.5	25.1	26.3	32.1	13.4	20.5	17.7	20.3
V	194	203	217	337	341	195	144	184	214	265
Cr	56.5	44.2	47.8	19.8	22.2	53.8	158	162	214	265
Co	34.7	37.5	38.3	23.1	24.8	33.8	20.6	30.9	28.9	20.2
Ni	66.4	84.6	76.4	25.4	27.1	66.6	89.1	114	75.5	7.02
Cu	96.49	236.4	256.7	205.4	208.9	114.20	/	/	/	/
Zn	48.0	44.1	49.0	94.9	103	44.1	/	/	/	/
Ga	12.0	11.1	11.2	14.7	13.6	12.0	/	/	/	/
Rb	0.589	1.420	1.070	3.130	3.270	0.583	4.9	18.1	22.0	17.2
Sr	971	1750	959	270	249	686	971	831	1118	776
Y	13.0	13.0	13.2	21.1	22.9	12.5	13.2	13.2	14.7	20.1
Zr	54.9	42.3	41.5	144	154	52.8	243	133	164	151
Nb	1.299	0.847	0.855	11.315	11.985	1.257	20.2	12.7	21.9	12.2
Cd	0.025	0.030	0.027	0.051	0.052	0.028	/	/	/	/
Sn	0.381	0.286	0.328	1.560	1.450	0.360	/	/	/	/
Cs	0.288	1.720	1.030	0.365	0.406	0.336	/	/	/	/
Ba	117	372	346	825	507	84.3	/	/	/	/
La	10.70	7.840	7.610	26.40	26.80	10.50	30.6	32.2	40.1	26.4
Ce	23.00	18.90	18.40	51.50	54.70	22.30	57.8	62.9	82.3	52.5
Pr	2.770	2.520	2.510	5.750	6.180	2.670	6.97	7.84	10.5	6.4
Nd	11.80	11.70	11.60	22.30	24.30	11.60	27.5	31.2	43.1	24.4
Sm	2.540	2.700	2.690	4.490	4.700	2.370	4.59	5.28	6.89	4.85
Eu	0.896	0.918	0.970	1.163	1.257	0.883	1.45	1.58	2.07	1.03
Gd	2.480	2.813	2.754	4.149	4.469	2.522	3.56	4.01	5.35	4.23
Tb	0.396	0.389	0.397	0.612	0.660	0.384	0.49	0.54	0.64	0.63
Dy	2.180	2.150	2.220	3.420	3.680	2.130	2.57	2.77	3.24	3.75
Ho	0.468	0.446	0.444	0.728	0.759	0.468	0.49	0.52	0.59	0.78
Er	1.350	1.230	1.240	2.120	2.290	1.310	1.32	1.37	1.45	2.25
Tm	0.190	0.169	0.175	0.304	0.328	0.194	0.19	0.2	0.2	0.34
Yb	1.210	1.050	1.120	1.960	2.110	1.210	1.25	1.23	1.24	2.13
Lu	0.174	0.164	0.165	0.291	0.323	0.173	0.20	0.17	0.17	0.34
Hf	1.390	0.941	1.040	3.290	3.510	1.460	5.37	3.27	4.16	3.72
Ta	0.084	0.062	0.051	0.597	0.644	0.079	1.35	0.68	1.16	0.68
W	0.151	2.09	1.50	2.75	1.88	0.33	/	/	/	/
Pb	0.394	0.206	0.200	45.20	35.10	0.417	8.13	8.07	4.18	21.06
Th	1.990	0.761	0.717	8.860	9.290	1.980	4.50	2.63	3.20	9.41
U	0.500	0.304	0.302	2.830	3.480	0.501	1.79	0.67	1.46	2.59

Notes: SP – serpentinite; G – gabbro; B – basalt; BA – basaltic andesite; / – under detection limit.
Data for samples 04Z06, 04Z26, 04Z29 and 04Z17 are from Niu *et al*. (2009*a*).

https://doi.org/10.1017/S0016756816000042 Published online by Cambridge University Press

Table 2. Sr–Nd isotopic compositions of the basalts from the Zhaheba area

Sample	Rock type	Rb (ppm)	Sr (ppm)	$^{87}Rb/^{86}Sr$	$^{87}Sr/^{86}Sr$ (1σ)	$(^{87}Sr/^{86}Sr)_i$	Sm (ppm)	Nd (ppm)	$^{147}Sm/^{144}Nd$	$^{143}Nd/^{144}Nd$ (1σ)	$(^{143}Nd/^{144}Nd)_i$	$\varepsilon_{Nd}(t)$
2013ALT01H3	Basalt (G2)	0.36	392	0.0027	0.704030(29)	0.704015	2.49	10.8	0.1394	0.512839(40)	0.512474	6.9
2013ALT01H10	Basalt (G2)	0.58	686	0.0024	0.704759(23)	0.704745	2.37	11.6	0.1235	0.512809(43)	0.512486	7.1
2013ALT03H1	Basalt (G1)	3.13	270	0.0335	0.706324(20)	0.706133	4.49	22.3	0.1217	0.512533(47)	0.512214	1.8
2013ALT03H2	Basalt (G1)	2.87	1320	0.0063	0.704289(20)	0.704255	4.95	28.6	0.1046	0.512719(51)	0.512445	6.3
2013ALT03H3	Basalt (G1)	8.06	516	0.0452	0.705368(43)	0.705111	5.97	36.9	0.0978	0.512707(30)	0.512450	6.4
2013ALT03H4	Basalt (G1)	9.65	1480	0.0189	0.704227(51)	0.704120	4.55	24.5	0.1123	0.512803(53)	0.512509	7.5

$\varepsilon_{Nd}(t) = 10\,000((^{143}Nd/^{144}Nd)_S(t)/(^{143}Nd/^{144}Nd)_{CHUR}(t)-1)$; $\varepsilon_{Nd}(t)$ and $(^{87}Sr/^{86}Sr)_i$ values of the basalts from the Zhaheba area are recalculated using the age of 401 Ma.

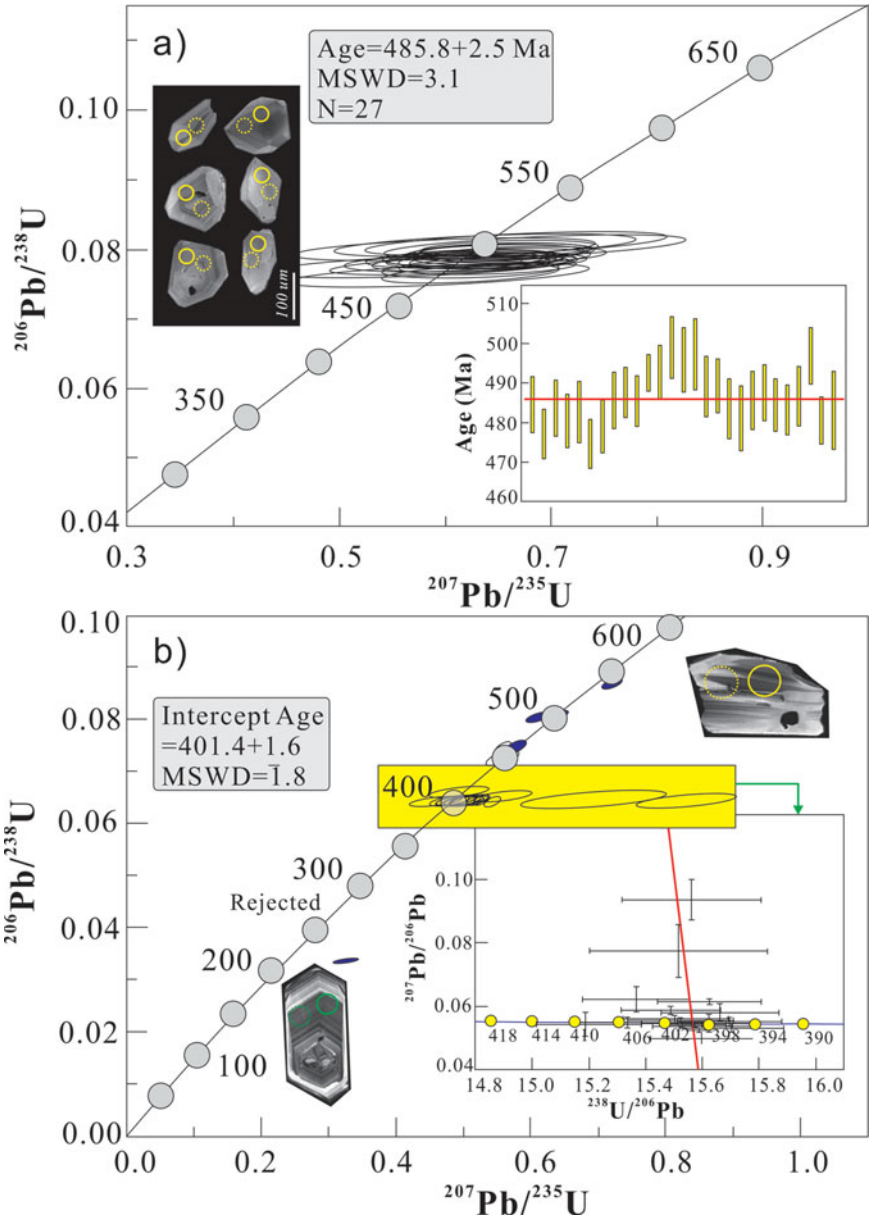

Figure 4. (Colour online) Concordia plots of U–Pb data for zircons from the gabbros of the Zhaheba ophiolite and the Devonian tuff. Error ellipses are at 1σ and age uncertainty is quoted at 2σ (mean) level.

(Fig. 4a; n = 27, MSWD = 3.1). This age is consistent with a previously reported 489 ± 4 Ma zircon SHRIMP U–Pb age for the layered gabbro from the Zhaheba ophiolite (Jian *et al.* 2003).

Zircons from the tuff sample are transparent and colourless, ranging from 100 to 200 μm in length with length/width ratios of 1–3. According to CL image features, the zircon grains can be divided into two groups. Group 1 (G1) zircons, accounting for about 70 % of the total zircons, display wide oscillatory or planar zoning, similar to those zircons crystallized from mafic magmas. The other group (G2) exhibit columnar forms and

https://doi.org/10.1017/S0016756816000042 Published online by Cambridge University Press

oscillatory zoning, sharing features with zircons crystallized from silicic magmas (G2, see inset of Fig. 4b). Twenty-nine analyses were performed on zircons from the tuff sample. Among these, eight spots on the G2 zircons yielded older ages ranging from 450 Ma to 500 Ma and are likely to be xenocrysts. The other 21 analyses performed on the G1 zircons yield consistent ^{206}Pb–^{238}U ages with a weighted mean age of 401 ± 2 Ma (MSWD = 3.3). Owing to the discordance between ^{206}Pb–^{238}U ages and ^{207}Pb–^{235}U ages, the Tera-Wasserburg inverse Concordia diagram yields a lower intercept age of 401.4 ± 1.6 Ma (MSWD = 1.8) (see insert of Fig. 4b), which is concurrent with the ^{206}Pb–^{238}U weighted mean age. This age is consistent with the fossils found in the carbonate (Xinjiang BGMR, 1993).

4.b. Mineral compositions

4.b.1. Spinel composition

Accessory chromian spinels occur in the serpentinite (Fig. 3d). Most grains are 100 to 300 µm across. The analytical results (online Supplementary Material Table S4 available at http://journals.cambridge.org/geo) show that the spinels have high Cr_2O_3, FeO and Al_2O_3 contents, variable MgO, and low NiO and TiO_2 contents. The mineral chemistry shows that these primary spinels are chromian spinels with Cr no. (100*Cr/(Cr + Al)) ranging from 44 to 60 and Mg no. (100*Mg/(Mg + Fe)) from 25 to 61. The compositional variation could be owing to either later stage melt/rock interactions and/or post-magmatic process (Oh *et al.* 2010). The uneven surface texture of the spinels observed under back-scattered electron (BSE) imaging suggests possible melt extraction before the emplacement of the mantle residue (Zhang *et al.* 2013).

4.b.2. Pyroxene compositions

The orthopyroxene is enstatite and has a rather homogeneous composition (En = 84–86). The clinopyroxenes in this study have very low TiO_2 contents (less than 0.5 %) and their chemical compositions are similar to that of diopside (online Supplementary Material Table S5 available at http://journals.cambridge.org/geo). The clinopyroxenes from the cumulates have consistent chemical compositions with 41–49 mol. Wo, 46–55 mol. En and 1–7 mol. Fs (Fig. 5a). They show non-alkaline rift-related features according to their Al_2O_3, SiO_2 and TiO_2 contents (Fig. 5b, c).

4.c. Whole-rock elemental geochemistry

4.c.1. Serpentinites and cumulates

The serpentinites have very high loss on ignition (LOI) (> 12 %, which is consistent with the intensive serpentinization) and low SiO_2 (less than 40 %), Al_2O_3 (mostly less than 1.0 %), K_2O (0.03–0.06 %), Na_2O (0.04–0.92 %) and TiO_2 (0.04–0.05 %). MgO and $Fe_2O_3^T$ contents yield Mg nos ranging from 89 to 91 (Table 1). On the Harker diagram, no significant correlation between Mg no. with other major elements is observed (Fig. 6). They have relatively high Cr (93–103 ppm) and low Ni contents (5–8 ppm) (Table 1). The high LOI (> 12 %) and low Na_2O, K_2O and CaO contents suggest significant hydrothermal alteration which altered the original content of some major elements (Na, K and Ca) as well as the large ion lithophile elements (LILEs) (e.g. Rb, Sr and Ba). However, since there is no marked correlation of LOI with MgO, Al_2O_3, $Fe_2O_3^T$ and TiO_2, we infer that there was no significant mobility of these elements during the hydrothermal alteration. Thus, these elements can be used for further discussions of petrogenesis. The serpentinites have very low total rare earth element (REE) and most high-field-strength element (HFSE) contents (Table 1). However, they show consistent U-shaped chondrite-normalized REE patterns (Fig. 7), sharing most features of harzburgites from ophiolite complexes (Pearce, 2014; both the chondrite and the primitive mantle values are from Sun & McDonough, 1989).

The gabbroic cumulates have SiO_2 ranging from 45.87 % to 51.27 %, and display variable $Fe_2O_3^T$ (3.24–4.68 %), Al_2O_3 (18.3–19.6 %, except sample 2013ALT01-3), CaO (9.54–15.42 %), TiO_2 (0.12–0.34 %), Na_2O (2.91–7.38 %, except sample 2013ALT01-3) and K_2O (0.11–0.46 %) owing to crystal fractionation and/or cumulation effects (Table 1).

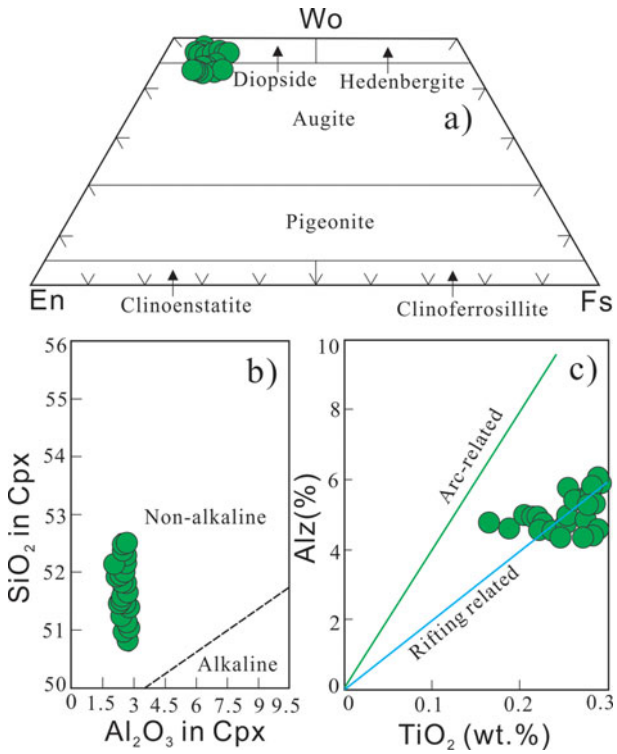

Figure 5. (Colour online) (a) Wo–En–Fs diagram showing the compositions of the clinopyroxene from gabbros from the Zhaheba ophiolite. (b) SiO_2 (wt %) v. Al_2O_3 (wt %) and (c) Al_{IV} (percentage of tetrahedral sites occupied by Al_Z) v. TiO_2 (wt %) in clinopyroxene from gabbros from the Zhaheba ophiolite.

https://doi.org/10.1017/S0016756816000042 Published online by Cambridge University Press

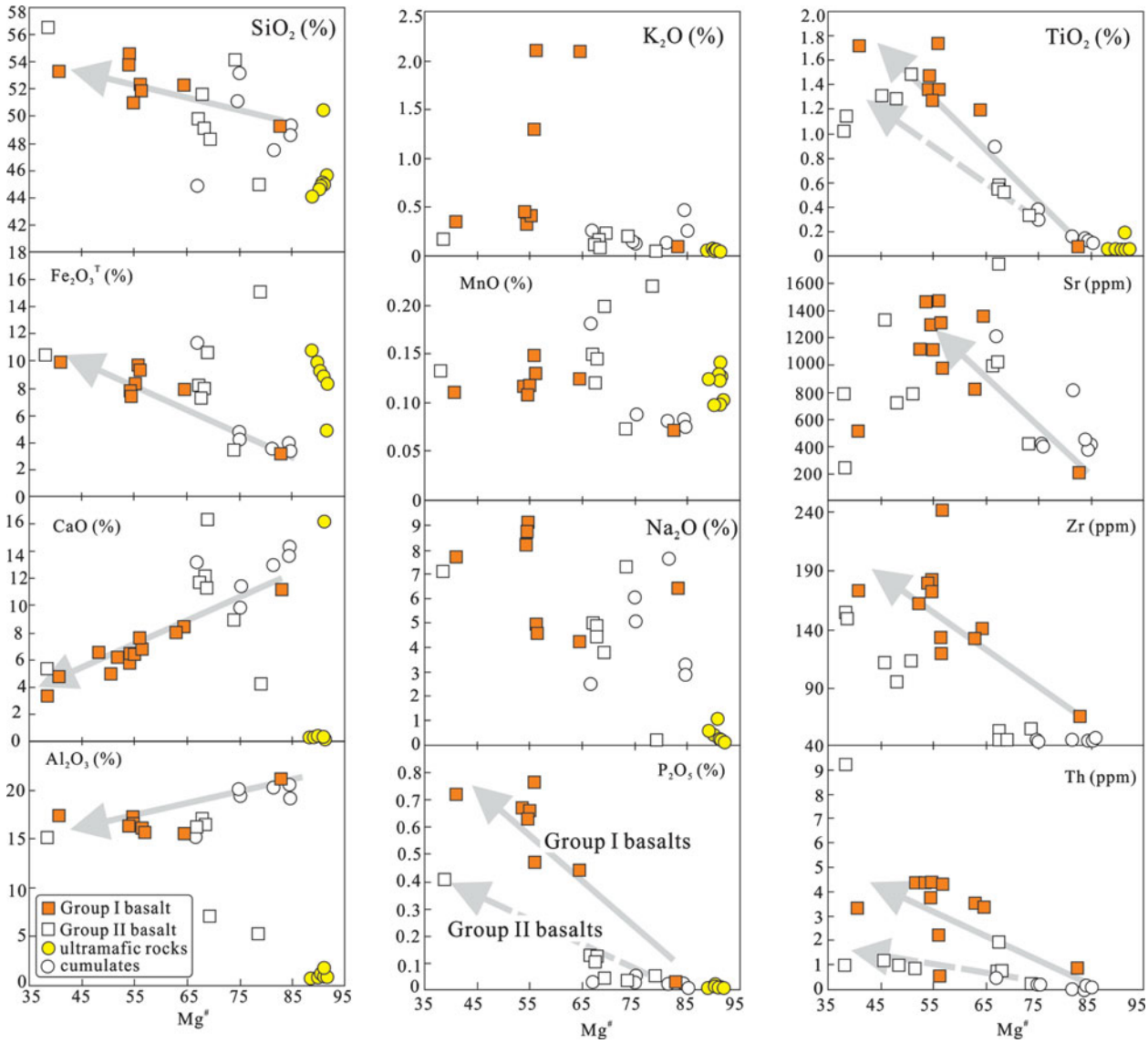

Figure 6. (Colour online) Harker variation diagram for the basalts and keratophyres (Mg no. v. SiO_2, Na_2O, K_2O, TiO_2, $Fe_2O_3^T$, Al_2O_3, CaO, Cr, Ni and Zr) (four samples reported by Niu *et al.* 2009*a* are also included for the major elements).

No significant correlation between Mg no. and major elements was observed on the Harker diagrams (Fig. 6). The cumulates have variable total REE contents ranging from 5 ppm to 41 ppm, and similar consistent chondrite-normalized REE patterns with light REE (LREE) enrichment ($(La/Yb)_N$ = 1.3–2.8) and pronounced positive Eu anomalies (Eu/Eu^* = 1.1–2.2). Sample 2013ALT01-3 shows a humped REE pattern, possibly due to the hornblende effect. The hornblendes are observed in the thin-section. On the primitive-mantle (PM) normalized incompatible element diagram (Fig. 7), all the cumulates are characterized by significant negative Nb anomalies (Nb/La = 0.2–0.4) and variable positive anomalies of Ba, Sr and Eu.

4.c.2. Basalts

The basalts and andesitic basalts have SiO_2 ranging from 43.15 % to 57.65 % (mostly less than 52 %, Table 1). Owing to variable hydrothermal alteration, only immobile incompatible elements were used for classification. On the Nb/Y v. Zr/TiO_2 diagram, the basalts can be divided into two subgroups, i.e. the alkaline Group 1 (G1) and subalkaline Group 2 (G2). Among the G2 samples, two samples straddle the boundary between basalt and andesite–basaltic andesite (Fig. 8a). Both G1 and G2 exhibit a tholeiitic trend on the FeO^T/MgO v. TiO_2 diagram (Fig. 8b). On the Harker diagrams, SiO_2, $Fe_2O_3^T$, P_2O_5, TiO_2, Sr, Zr and Th increase while CaO and Al_2O_3 decrease with decreasing Mg no. for the G1 basalts. As for the G2 basalts, P_2O_5, TiO_2, Zr and Th increase with deceasing Mg no. (Fig. 6).

The G1 basalts have relatively high total REE contents ranging from 124 ppm to 205 ppm while the G2 basalts have 50 ppm to 60 ppm total REEs. G1 basalts have elevated LREEs with $(La/Yb)_N$ between 10 and 30 (mostly above 20) and show moderate negative to

https://doi.org/10.1017/S0016756816000042 Published online by Cambridge University Press

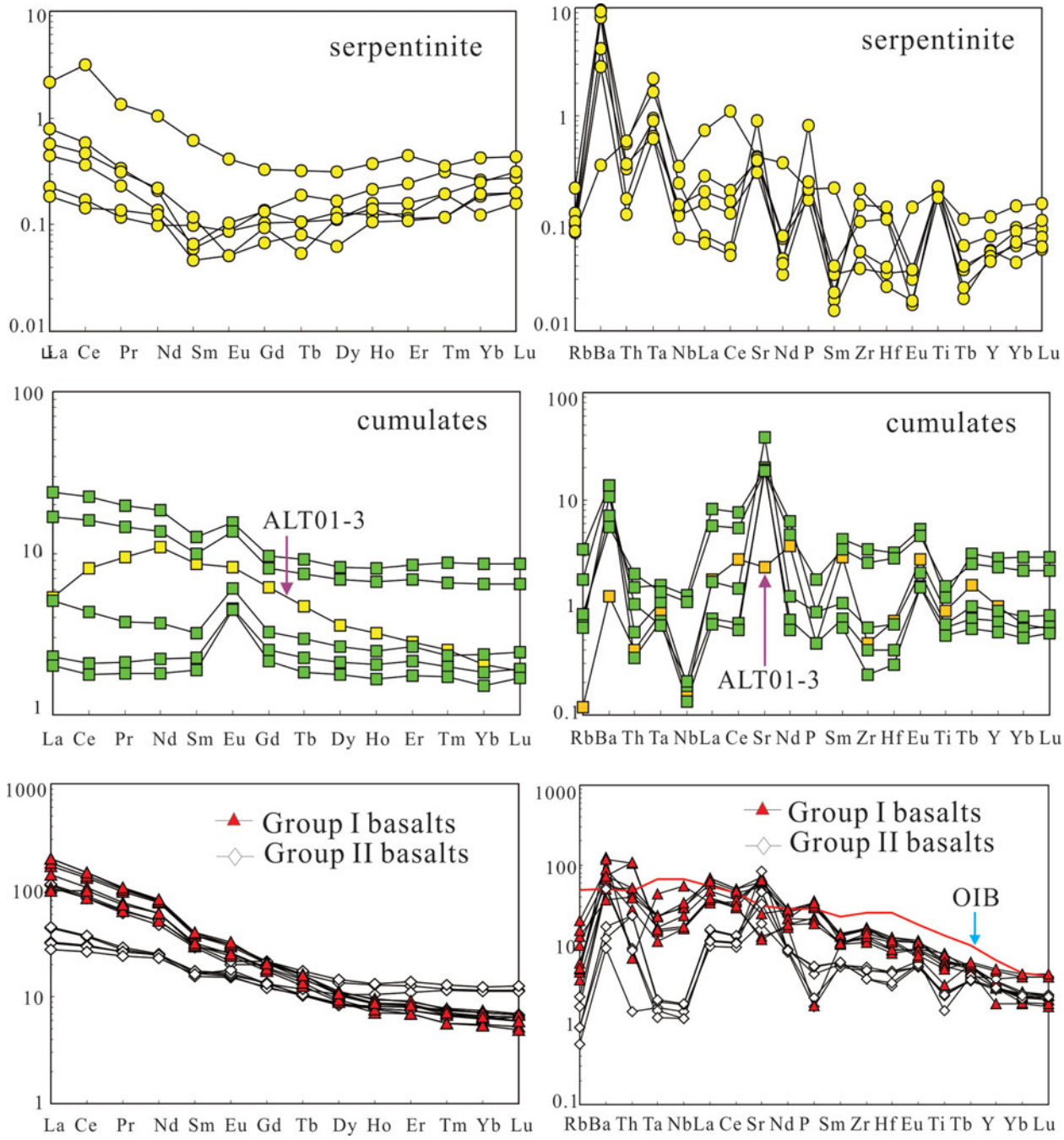

Figure 7. (Colour online) Chondrite-normalized REE patterns and primitive mantle-normalized incompatible trace-element multi-element diagrams for the serpentinite and gabbros from the Zhaheba ophiolite and the Devonian basalts. The normalization values are from Sun & McDonough (1989).

slight positive Eu anomalies ($Eu/Eu^* = 0.70–1.14$) (Fig. 7). The G2 basalts have relatively flat REE patterns with $(La/Yb)_N$ ranging from 4 to 6 and slight positive Eu anomalies ($Eu/Eu^* = 1.02–1.21$) (Fig. 7). On the PM-normalized multi-element diagrams, the G1 basalts show humped patterns with variable negative Nb–Ta anomalies with Nb/La ranging from 0.44 to 0.87, and negative to slight positive Sr anomalies consistent with their Eu anomalies. The G2 basalts have lower incompatible element contents than those of the G1 basalts and display pronounced negative Nb–Ta anomalies with very low Nb/La ratios (~0.11). All these features resemble those of typical arc basalts (Fig. 7).

4.d. Whole-rock Sr–Nd and zircon Hf–O isotopes

Strontium and neodymium isotopic compositions of the representative basalts are listed in Table 2. G1 basalts and G2 basalts have similar Sr–Nd isotopic compositions. They show a narrow range of $^{87}Rb/^{86}Sr$ ratios (0.0024–0.0452) and $^{87}Sr/^{86}Sr$ ratios (0.704030–0.705368), corresponding to relatively homogeneous initial $^{87}Sr/^{86}Sr$ ratios (0.704015–0.705111, except for 2013ALT03H1). They have $^{147}Sm/^{144}Nd$ ratios between 0.0978 and 0.1394 and $^{143}Nd/^{144}Nd$ ratios between 0.512707 and 0.512839 and nearly constant $\varepsilon_{Nd}(t)$ values from +6.3 to +7.5 (except 2013ALT03H1 that is +1.8).

https://doi.org/10.1017/S0016756816000042 Published online by Cambridge University Press

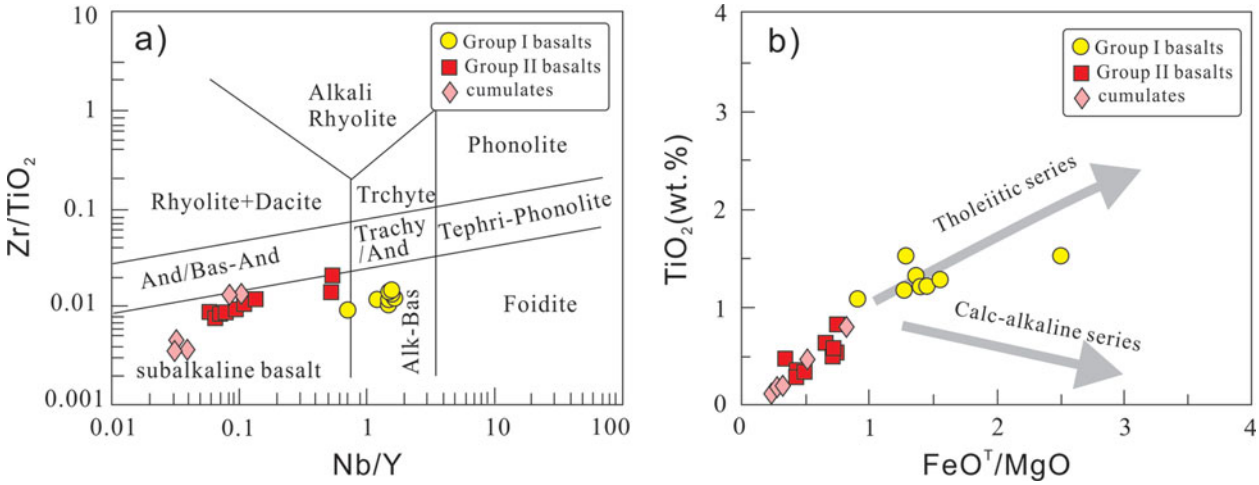

Figure 8. (Colour online) (a) Incompatible element (Zr/TiO_2 v. Nb/Y) classification diagram for the Devonian basalts and gabbros (Winchester & Floyd, 1977). (b) Whole-rock TiO_2 v. FeO^T/MgO plots for discrimination between the calc-alkaline and tholeiitic series. The calc-alkaline and tholeiitic trends are after Miyashiro (1974).

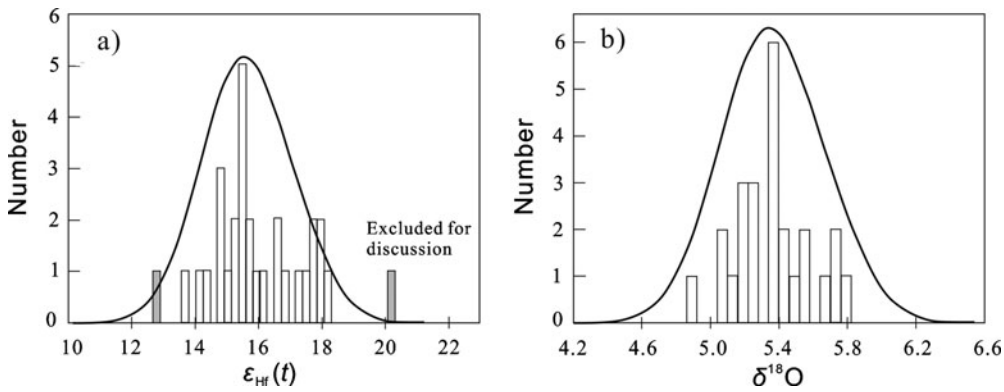

Figure 9. (a) Zircon $\varepsilon_{Hf}(t)$ and (b) O isotope spectra for the gabbros from the Zhaheba ophiolite.

Zircon Hf isotope compositions of the cumulate sample (2013ALT01) show consistent results (online Supplementary Material Table S2 available at http://journals.cambridge.org/geo; Fig. 9a), with ε_{Hf} (t = 485 Ma) ranging from 13 to 20. The Hf model ages range from 285 Ma to 588 Ma. Some spots yield high $\varepsilon_{Hf}(t)$ (> 16) and their T_{DM} ages are younger than the crystallization age for unknown reasons, and these spots are excluded from further discussions. On the histogram of $\varepsilon_{Hf}(t)$, the analyses show nearly a Gaussian distribution peaking at 15.7. The measured $\delta^{18}O$ values range from 4.91 ‰ to 5.73 ‰, also forming a Gaussian distribution (Fig. 9b). Thus, these zircons have homogeneous oxygen isotopic compositions with a mean $\delta^{18}O_{zircon}$ value of 5.37 ± 0.23 ‰ (Fig. 9b).

Zircons of ~400 Ma from the tuff sample have a large range of $\varepsilon_{Hf}(t)$ values between 1.4 and 9.2 with single-stage Hf model ages ranging from 680 Ma to 920 Ma. The xenocrysts have variable Hf isotope compositions sharing the features of detrital and igneous zircons from the Altai region (Sun *et al.* 2008).

5. Discussion

5.a. The individual members of the Zhaheba ophiolite

According to the zircon U–Pb ages of the cumulates and the volcanic rocks, the cumulates and the Devonian lavas were emplaced and erupted at *c.* 486 Ma and 401 Ma, respectively. The age of the cumulate is broadly consistent with the previously reported age (503 ± 7 Ma) of the Almantai ophiolite in the southeastern section of the Zhaheba ophiolite and the age (416 ± 3 Ma) of the Kelameili ophiolite to south of the Zhaheba–Almantai ophiolite complex (Huang *et al.* 2012; Xiao *et al.* 2009*b*, Fig. 1). The volcanic sequences (401 Ma) and the cumulates (486 Ma) (including the serpentinites) are clearly asynchronous. Thus, we suggest that the volcanic sequences are not a member of the Zhaheba ophiolite. The Devonian fossils are consistent with the zircon U–Pb age for the volcanic sequence (Xingjiang BGMR, 1993).

According to the ages of the ophiolites in eastern Junggar and the southern side of the Altai terrane (Fig. 1b), the ophiolites can be subdivided into three stages, i.e. the Cambrian Zhaheba–Almantai opiolitic

https://doi.org/10.1017/S0016756816000042 Published online by Cambridge University Press

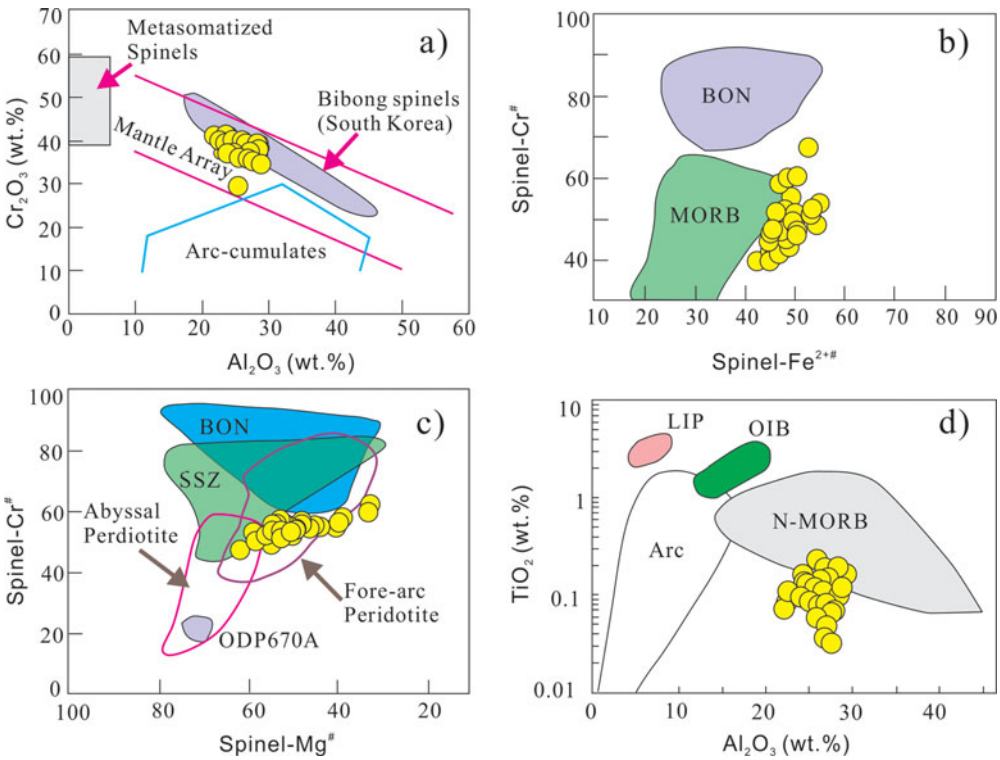

Figure 10. (Colour online) Plot of chromian spinels on discrimination diagrams. (a) Cr_2O_3 versus Al_2O_3 (wt %) diagram (after Franz & Wirth, 2000). (b) Cr no. (100*Cr/(Cr+Al)) versus Fe^{2+} no. (100*Fe^{2+}/(Fe^{2+}+Mg)) of spinels from the Zhaheba ophiolite (after Arai, 1994; Barnes & Roeder, 2001). (c) Cr no. (100*Cr/(Cr+Al)) versus Mg no. (100*Mg/(Mg+Fe)) of spinels from the Zhaheba ophiolite (after Monnier *et al.* 1995). (d) TiO_2 versus Al_2O_3 compositional relationships in spinel from the Zhaheba ophiolite (after Kamentsky, Crawford & Meffre, 2001). BON – boninites; MORB – mid-ocean ridge basalts; SSZ – supra-subduction zone basalts.

mélange (500–480 Ma) (Jian *et al.* 2003; Luo *et al.* 2015; this study), the Devonian Kelameili ophiolitic mélange (430–400 Ma) (Xiao *et al.* 2009*b*, 2014 and references therein) and the Carboniferous Kuerti complex (370–350 Ma) (Zhang *et al.* 2003; Wu *et al.* 2006).

5.b. Origin of the serpentinite and cumulates

Studies on ultramafic rocks have confirmed that Cr-spinel serves as a potential petrogenetic and tectonic indicator based on its ability to survive during later metamorphism (Hellebrand, Snow & Mühe, 2002; Oh *et al.* 2010). Generally the Cr no. of Cr-spinel does not undergo any significant change during subsolidus recrystallization (Arai, 1994); therefore, it can be used to determine the degree of partial melting experienced by Cr-spinel-bearing peridotites (Dick & Bullen, 1984; Hellebrand *et al.* 2001). On the Cr_2O_3 (wt %) v. Al_2O_3 (wt %) diagram, all the analysed spots plot within the mantle array, similar to those of the Bibong ultramafic bodies in South Korea and ultramafic members of the ophiolites in the Tethys orogenic belt (Fig. 10a) (Oh *et al.* 2010). Fe^{2+} no. increases with increasing Cr no., though they deviate a little from the mid-ocean ridge (MORB) spinel field (Fig. 10b). Positive correlation between Mg no. and Cr no. was observed, and most spinels plot in the fore-arc peridotite field with some in the overlapping region between fore-arc peridotite and abyssal peridotite (Fig. 10c). The TiO_2 content of spinel in the magma varies with the tectonic environment of magma separation. Generally, TiO_2 is extremely low in arc/back-arc magma, intermediate in mature mid-ocean ridge magma and high in intraplate magma (Arai, 1994; Pearce, 2008). Jan & Windley (1990) suggested that Alaskan-type complexes and mafic–ultramafic rocks from deeper levels of island arcs generally contain > 0.3 % TiO_2. Spinels from peridotite genetically related to large igneous provinces (LIP) or ocean island basalts (OIB) have higher TiO_2 contents and higher Al_2O_3 contents than those of the spinels from SSZ-type ophiolites. On the TiO_2 v. Al_2O_3 diagrams, most spinels from the serpentinite show MORB affinity, and some have lower TiO_2 contents than those spinels from MORB-type ophiolites (Fig. 10d).

The major and trace elements of the gabbroic cumulates are constrained by crystal fractionation and cumulation. According to their REE distribution patterns and the incompatible element diagrams (Fig. 7), the positive Eu and Sr anomalies could be due to the cumulation of plagioclase. Thus, we only use the incompatible element ratios, mineral compositions and isotope compositions to decipher its mantle sources.

First of all, the zircons from the gabbroic cumulates have high $\varepsilon_{Hf}(t)$ values (about +16 at 485 Ma), which are above the depleted mantle evolution line. The average $\delta^{18}O$ value of these zircons is 5.37 ‰, consistent with the normal mantle zircon value of 5.3 ‰ (Valley *et al.* 1998). These features show that the

https://doi.org/10.1017/S0016756816000042 Published online by Cambridge University Press

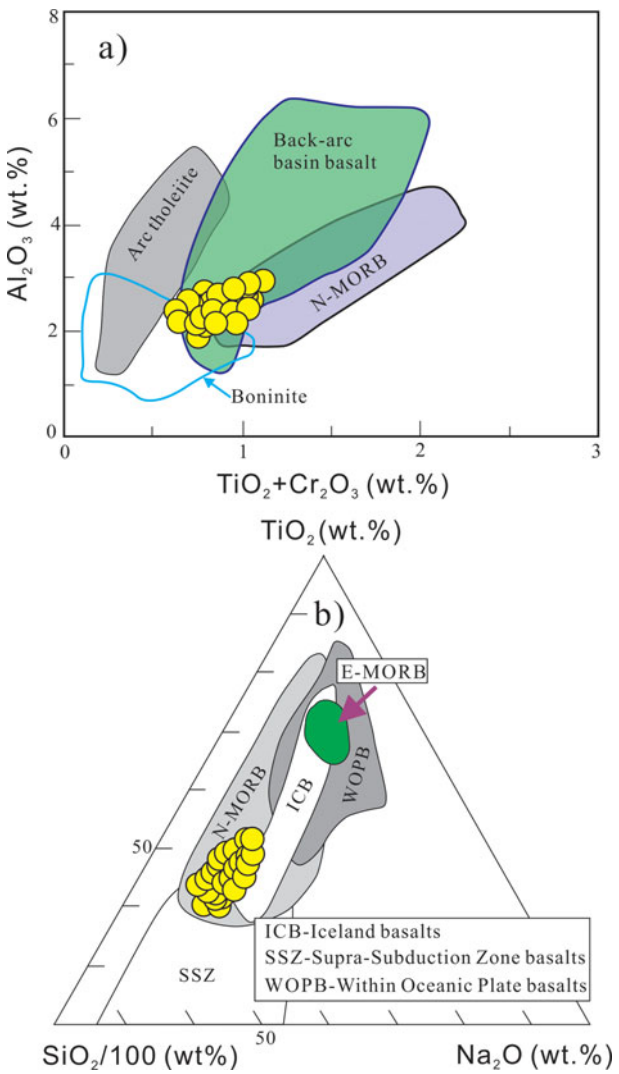

Figure 11. (Colour online) (a) Al_2O_3 v. $TiO_2 + Cr_2O_3$ diagram and (b) TiO_2–SiO_2/100–Na_2O triangle diagram of clinopyroxene from the gabbro of the Zhaheba ophiolite, with all the analysed spots plotting in the overlap area between N-MORB and back-arc basin basalt and overlapping between the SSZ-type and N-MORB.

zircons of the gabbroic cumulates crystallized from mafic magma derived from highly depleted mantle sources (DMM-type). The isotope features argue that the cumulates crystallized from basalts that were derived from depleted asthenospheric mantle sources, similar those of mafic sheets from MORB-type ophiolite complexes. On the other hand, as shown in Figure 5c, the clinopyroxenes from the cumulates exhibit rift-related trends. On the Al_2O_3 v. $TiO_2 + Cr_2O_3$ diagram, all the analysed clinopyroxene spots plot in the overlap area between N-MORB and back-arc basin basalt (Fig. 11a). On the SiO_2/100–TiO_2–Na_2O diagram, most compositions plot into the MORB field with some overlapping between the SSZ-type and N-MORB fields (Fig. 11b). Note that the gabbroic cumulates have significant Nb–Ta troughs on the PM-normalized diagrams and some samples exhibit slight LREE enrichment (Fig. 7). There are two possibilities. One is crustal contamination, particularly by marine sediments. However, there is no correlation between Nb/La and Nb/Th ratios (Fig. 12a), which rules out significant crustal contamination. Moreover, the single-stage Hf model age is similar to the crystallization age of the gabbro. The other possibility is that the mantle source underwent subduction-related metasomatism. However, their Nb/Zr and Th/Zr ratios are similar to MORB and exhibit neither fluid nor melt-related metasomatism trends (Fig. 12b). Therefore, the significant Nb–Ta negative anomalies in the clinopyroxenes are not necessarily related to subduction-related metasomatism. Niu *et al.* (2002) have pointed out that the significant Nb–Ta negative anomalies of the gabbros from the Southwest Indian Ridge are possibly controlled by both the compositions and modes of the constituent minerals (such as magnetite or ilmenite). Thus, we deduce that the gabbro represents a cumulate part of the ocean ridge lithosphere which did not undergo crustal contamination or subduction-related metasomatism.

5.c. Petrogenesis of the Devonian basalts

According to their geochemistry, the basalts are divided into two subgroups, i.e. alkaline G1 and tholeiitic–calc-alkaline G2. G1 basalts have high Nb (11–24 ppm, mostly above 15 ppm), P_2O_5 (0.4–0.6 %) and Nb/U ratios (11–15, with some up to 60) and variable $(La/Yb)_N$ and Yb values, suggesting they are Nb-rich basalts (NEBs) (Defant, Jackson & Drummond, 1992; Polat & Kerrich, 2001) (Fig. 13). Two alternative mantle sources have been proposed to account for the origin and distinctive geochemical features of NEBs: (1) an OIB mantle or enriched mantle component occurring in the mantle wedge (e.g. Castillo, Solidum & Punongbayan, 2002); (2) a mantle wedge which was metasomatized by adakites (Defant, Jackson & Drummond, 1992; Defant & Drummond, 1993; Sajona *et al.* 1996). The later mechanism likely played an important role in the petrogenesis of the G1 basalts.

Previous studies demonstrated that NEBs may be derived from a source composed of OIB-like enriched mantle (Castillo, Rigby & Solidum, 2007; Hastie *et al.* 2011). However, the G1 NEBs have low initial $^{87}Sr/^{86}Sr$ values (0.704120–0.706133) and high $\varepsilon_{Nd}(t)$ values (+1.8 to +7.5). They are different from enriched OIBs. In addition, the NEBs have lower Nb/U (3.44–20.4) and higher La/Nb (1.51–2.54) ratios than OIBs (e.g. Zindler & Hart, 1986). Therefore, these characteristics rule out an OIB mantle source. Alternatively, we suggest that the G1 NEBs are possibly derived from a mantle wedge metasomatized by adakite-like melts derived from a hot subducted slab (Sajona *et al.* 1996; Keppler, 1996). Slab melting generates liquids of adakite composition. Some of these erupted as rhyolites, whereas others reacted with mantle peridotite to generate a HFSE-enriched source (Hollings & Kerrich, 2000). This model requires that adakites and NEBs are erupted more or less simultaneously (Defant, Jackson & Drummond, 1992; Sajona *et al.* 1996). Zhang *et al.* (2008) reported Devonian adakites along the northern

https://doi.org/10.1017/S0016756816000042 Published online by Cambridge University Press

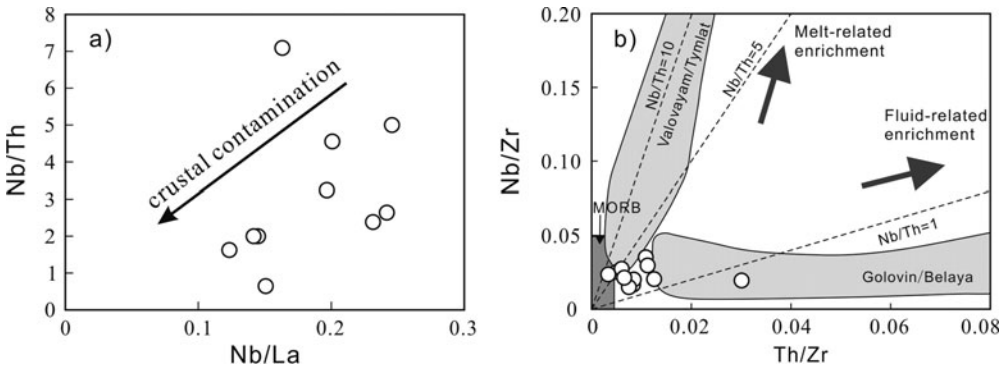

Figure 12. (a) Nb/Th v. Nb/La diagram showing the crustal contamination and (b) plot of Nb/Zr v. Th/Zr diagram for the gabbro cumulates of the Zhaheba ophiolite.

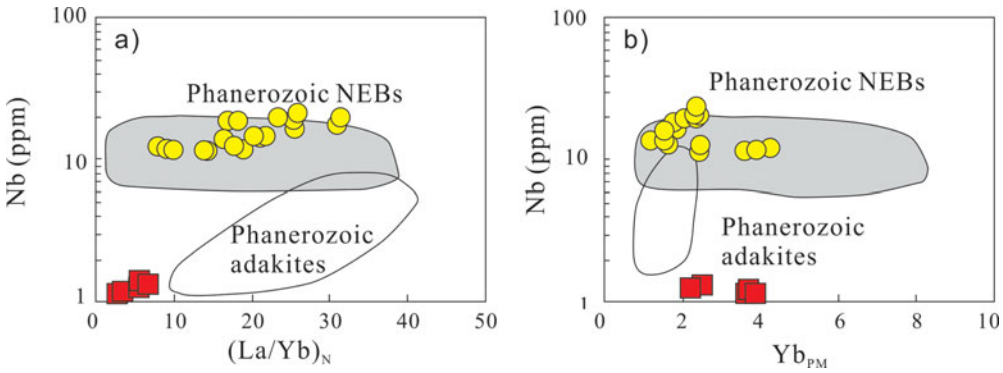

Figure 13. (Colour online) (a) $(La/Yb)_N$ and (b) Yb_{PM} v. Nb diagrams for the basalts from the Zhaheba area, indicating that G1 basalts have features of Nb-enriched basalts (NEBs).

margin of the Junggar. The G1 NEBs have varying $\varepsilon_{Nd}(t)$ (1.8–7.5) and $(^{87}Sr/^{86}Sr)_i$ (0.704120–0.706133) values, which indicates that their source was compositionally heterogeneous (Table 2). The relatively low $\varepsilon_{Nd}(t)$ values and high $(^{87}Sr/^{86}Sr)_i$ ratios indicate that they underwent assimilation of old crustal materials. This is consistent with significant P and Ti troughs on the PM-normalized diagrams. Thus, the G1 basalts in the Zhaheba area were most likely derived from partial melting of a mantle wedge previously metasomatized by adakitic melts released from a subducted hot slab. Some samples underwent significant assimilation of old crustal materials.

The G2 basalts have high LILE contents and relatively low TiO_2, Nb and other HFSE contents, and low Nb/La (< 0.3), Nb/Y and FeO^T/MgO ratios (Fig. 8), reflecting the metasomatism of mantle sources by the influx of slab-released fluids and/or melts derived from partial melting of the subducted slab (Saunders, Norry & Tarney, 1991; Stern, 2002). This scenario shares most features of arc basalts. On the other hand, the G2 basalts have low $(Hf/Sm)_{PM}$ (0.7–1.0), $(Ta/La)_{PM}$ (0.1–0.2) and Nb/Th (0.6–1.0) ratios, indicating the mantle source for the G2 basalts was mainly metasomatized by fluids related to oceanic crust subduction (Hofmann & Jochum, 1996). Compared with the G1 NEBs, the G2 basalts have low P_2O_5 contents and Nb/U and $(Nb/Th)_{PM}$ ratios (Table 1; Fig. 14). They all plot in the fields of typical island arc volcanic rocks (Fig. 14). Thus, the G2 basalts derived from partial melting of a mantle wedge previously metasomatized by fluids released from a subducted slab. In the field, the G1 and G2 basalts are interbedded with each other. The field observation indicates that they share a common tectonic setting, which is consistent with their petrogenesis.

5.d. Implications for the Palaeozoic accretion process in eastern Junggar

There are three ophiolitic belts in the eastern Junggar, i.e. the Kelameili ophiolite (416 Ma; Hu *et al.* 2014; Fang *et al.* 2015), Zhaheba–Almantai ophiolite (503–485 Ma; Jian *et al.* 2003; Luo *et al.* 2015; this study) and the Fuyun ophiolite (400 Ma) (Fig. 1b). According to the mineral chemistry and geochemistry of the Almantai and Kelameili ophiolites (Hu *et al.* 2014), they were formed in mid-ocean ridge rather than subduction-related settings.

Both the geochemistry and field observations reveal that the Cambrian–Devonian volcanic–sedimentary sequences along the eastern Junggar represent diverse tectonic settings, including intra-oceanic arc, seamount, accretionary wedge, mid-ocean ridge and deep-sea flysch (Niu *et al.* 2007, 2009*a*,*b*; Xiao *et al.* 2009*a*). Previous work suggests that the tectonic setting of East Junggar can be defined as intra-oceanic island arc (Xiao *et al.* 2009*b*). According to the elemental

https://doi.org/10.1017/S0016756816000042 Published online by Cambridge University Press

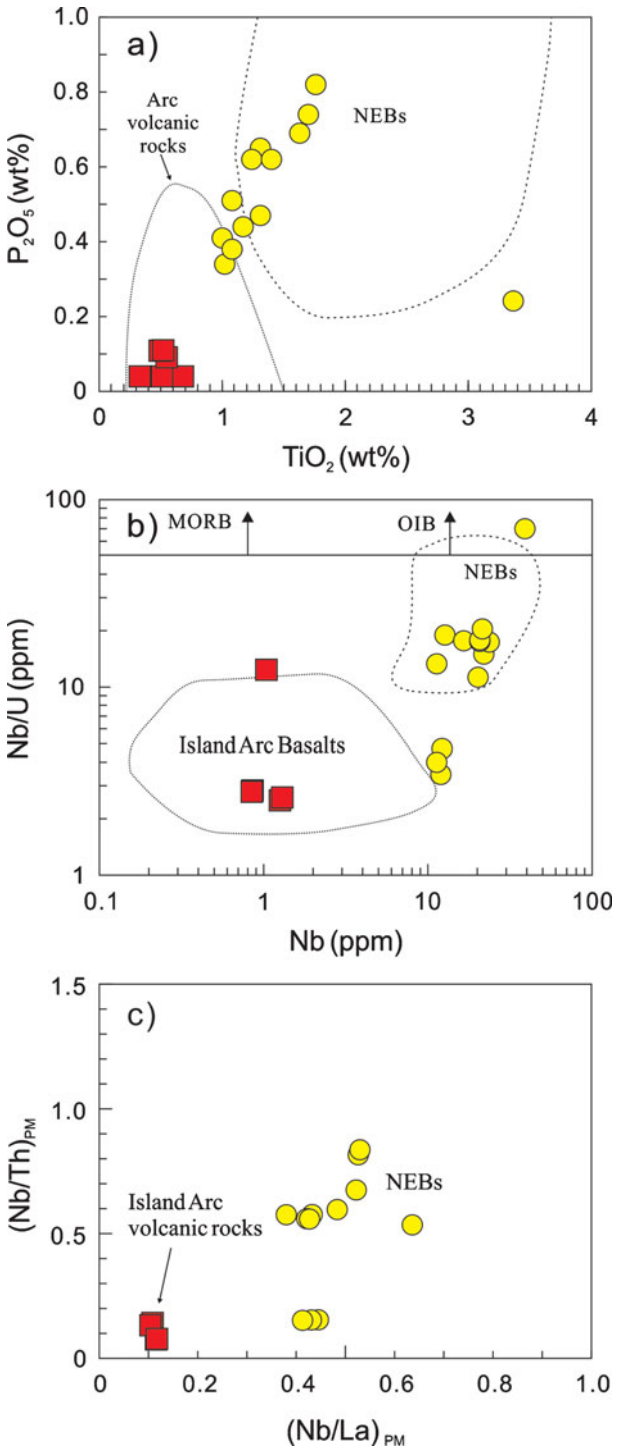

Figure 14. (Colour online) (a) P_2O_5 versus TiO_2 diagram. (b) Nb/U versus Nb diagram. (c) $(Nb/Th)_{PM}$ versus $(Nb/La)_{PM}$ diagram. Fields for arc volcanic rocks and Nb-enriched arc basalts (NEBs) are from Defant, Jackson & Drummond (1992) and Schiano *et al.* (1995), respectively.

and isotope geochemistry, the ultramafic end member of the Zhaheba–Almantai ophiolite was formed at a mid-ocean ridge. Also, the cumulates derived from asthenospheric mantle and are similar to the gabbros from the mid-ocean ridge.

Recently, Ye *et al.* (2015) identified a Devonian Alaskan-type mafic intrusive belt emplaced during 400–380 Ma along the southern margin of the Altai orogen. On the other hand, the ages of the granitoids along the southern margin of the Altai orogen were dated at 460–375 Ma with a peak at *c.* 400 Ma (Wang *et al.* 2006, 2009; Tong *et al.* 2007; Yuan *et al.* 2007; Sun *et al.* 2008, 2009; Zhang *et al.* 2012; Ye *et al.* 2015). Most of these granitoids show typical I-type granite features, and both whole-rock Nd and zircon Hf isotopes suggest that these granitoids were mainly derived by partial melting of juvenile crust with variable involvement of mantle contributions (Chen & Jahn, 2002; Wang *et al.* 2009). The Devonian Alaskan-type mafic rocks and I-type granites are interpreted as a continental magmatic arc along the southern margin of the Altai orogen and northward subduction along the Iritish zone (Ye *et al.* 2015).

As mentioned before (see Section 5.c), the Nb-enriched G1 basalts and the typical arc-signature G2 basalts in the Zhaheba area represent young oceanic slab subduction along the Iritish area. In the tectonic sketch, this is assigned to the Dulate arc system (Figs 1b, 15). Niu *et al.* (2007, 2009*b*) reported ultrahigh-pressure metamorphism, such as the supersilicic garnet and supersilicic pyroxene within the Zhaheba ophiolite complex. Ophiolite, ultrahigh-pressure metamorphic rocks and the Nb-enriched basalts compose a tectonic mélange along the southern margin of the Iritish suture zone (Niu *et al.* 2008). Similar tectonic mélanges have been identified in other orogens (Furnes, Pedersen & Hertogen, 1991; Ota, Utsunomiya & Uchio, 2007; Xiao *et al.* 2013).

We constructed a cartoon model showing the tectonic evolution of the eastern Junggar terrane (Fig. 15).

(1) During Cambrian time (*c.* 500 Ma), the Palaeo-Asian Ocean subducted northwards beneath the Chinese Altai arc. During this period, a new intra-oceanic subduction zone was initiated and the intra-oceanic arc and accretionary wedge were formed (Fig. 15a). At the same time, the northward subduction along the Iritish zone started, and several arc basalts and scarce arc-signature granites formed in the Altai terrane.

(2) From late Cambrian to early Ordovician time (500–480 Ma), the peridotite was scraped off from the mid-ocean ridge at the fore-arc and the Zhaheba–Almantai ophiolite accreted to the accretionary wedge (Fig. 15b). During this time, accretionary complex and arc-affinity rocks were formed along the southern margin of the Altai terrane during continued northward subduction.

(3) During late Ordovician to Silurian time (480–420 Ma), the high-Mg diorite (458 Ma; Luo *et al.* 2015) intruded the intra-oceanic arc. The Suoerkuduke adakitic andesitic and Nb-enriched basaltic lavas (440 Ma; Shen *et al.* 2014) were formed. The Nb-enriched basalts were generated as a result of partial melting of a mantle wedge previously metasomatized by adakitic melts released from this subducted hot slab (Fig. 15c). At the same time, another intra-oceanic subduction zone started, and a new intra-oceanic arc was formed.

https://doi.org/10.1017/S0016756816000042 Published online by Cambridge University Press

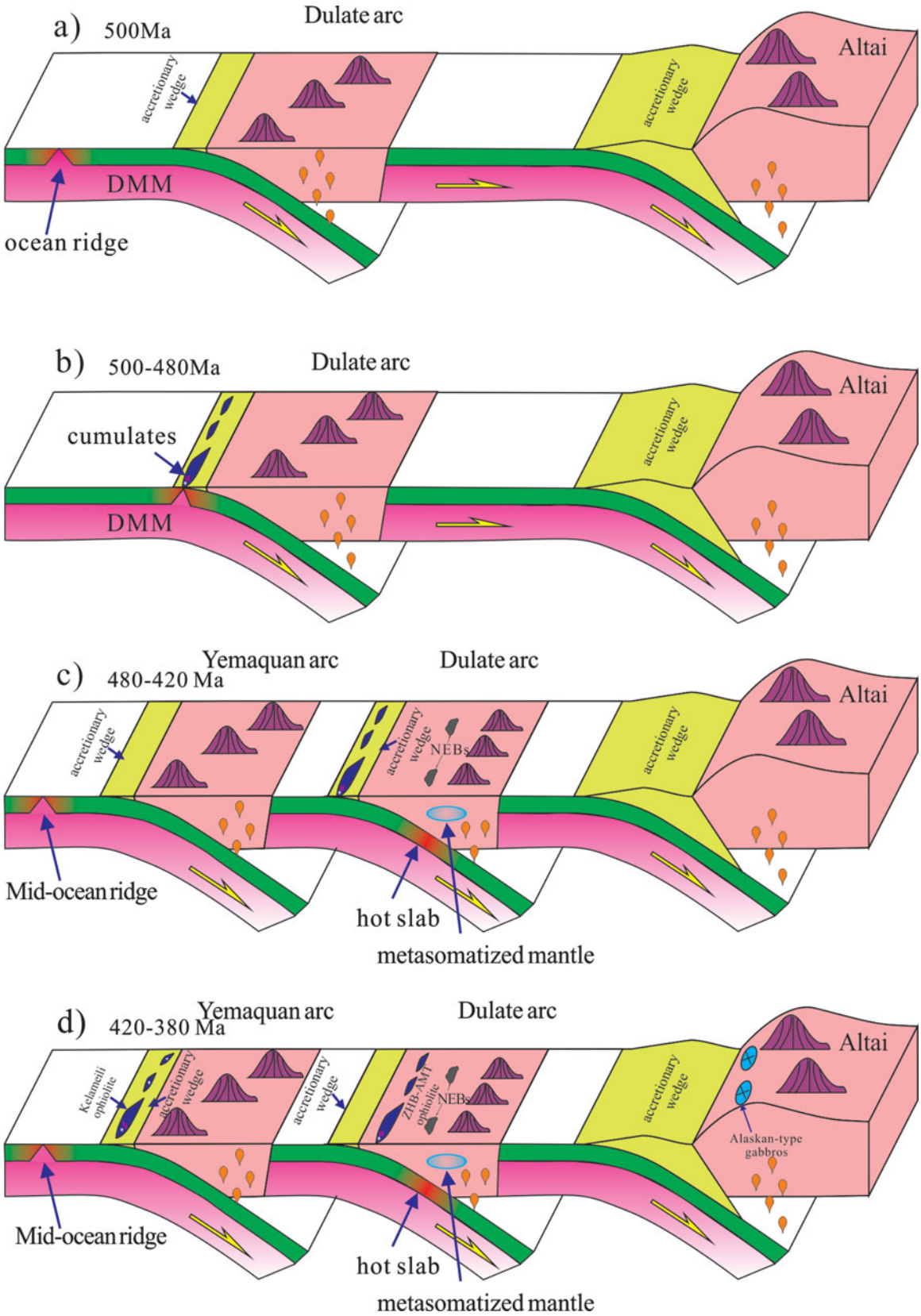

Figure 15. (Colour online) Cartoon illustrating the formation of the ophiolite complexes in eastern Junggar and the accretion process of the Junggar terrane.

https://doi.org/10.1017/S0016756816000042 Published online by Cambridge University Press

(4) The Kelameili ophiolite formed in a MORB setting from Silurian to Devonian times (420–380 Ma) (Hu *et al.* 2014; Fang *et al.* 2015). At this time the former intra-oceanic subduction still continued. Also, the G1 basalts (NEBs) and G2 basalts erupted owing to partial melting of a mantle wedge previously metasomatized by fluids released from a young, hot subducting slab and adakitic melts, respectively (Fig. 15d). The Alaskan-type mafic rocks and I-type granites occurred as a continental magmatic arc along the southern margin of the Altai orogen, and northward subduction occurred along the Iritish zone from Devonian to early Carboniferous times (400–380 Ma). The whole Junggar Ocean most likely closed by middle to late Carboniferous times, because in eastern Junggar, as well as in western Junggar and the southern Altai orogeny, the late Carboniferous–Permian magmatism has typical post-orogenic or intraplate geochemical features and the Permian sedimentary sequences in Junggar exhibit continental facies.

6. Conclusions

(1) The cumulate of the Zhaheba ophiolite crystallized at ~485 Ma, while the basalts in this area erupted at *c.* 400 Ma. Thus, the basalt sequence and the cumulates are asynchronous and the basalts are not a member of the Zhaheba–Almantai ophiolite. The basalts were generated owing to partial melting of a mantle wedge metasomatized by fluids released from a subducting slab or adakitic melts produced by slab melting.

(2) The cumulate derived from asthenospheric mantle and is similar to the gabbros from the Southwest Indian Ridge. The ultramafic end members of the Zhaheba ophiolite represent residual asthenosphere mantle at a mid-ocean ridge. Their mineral chemistry suggests that the Zhaheba–Almantai ophiolite was MORB-type.

(3) The Zhaheba–Almantai ophiolite accreted to the accretionary wedge along the southern margin of the Iritish suture zone during the roll-back of the subduction zone from north to south. The Kelameili ophiolite was a member of an intra-oceanic accretionary wedge in the Junggar Ocean. The eastern Junggar is a typical Phanerozoic accretionary orogenic belt comprising ophiolites, a seamount, intra-oceanic arc and possible deep-sea flysch.

Acknowledgements. Mr Ru-Fu Ding is thanked for his assistance during the field trip. We really appreciate Prof. Huai-Kun Li for his assistance with zircon U–Pb age and Hf isotope analyses. We are very grateful to Dr Phil Leat and Prof. Wenjiao Xiao for their very constructive reviews that significantly improved the quality of this manuscript. This study is financially supported by the National 305 Project of China (2011BAB06B03-01).

Supplementary material

To view supplementary material for this article, please visit http://dx.doi.org/10.1017/S0016756816000042.

References

ARAI, S. 1994. Characterization of spinel peridotites by olivine–spinel compositional relationships: review and interpretation. *Chemical Geology* **113**, 191–204.

BARNES, S. J. & ROEDER, P. L. 2001. The range of spinel compositions in terrestrial mafic and ultramafic rocks. *Journal of Petrology* **42**, 2279–302.

CASTILLO, P. R., RIGBY, S. J. & SOLIDUM, R. U. 2007. Origin of high field strength element enrichment in volcanic arcs: geochemical evidence from the Sulu Arc, southern Philippines. *Lithos* **97**, 271–88.

CASTILLO, P. R., SOLIDUM, R. U. & PUNONGBAYAN, R. S. 2002. Origin of high field strength element enrichment in the Sulu Arc, southern Philippines, revisited. *Geology* **30**, 707–10.

CAWOOD, P. A., KRÖNER, A., COLLINS, W. J., KUSKY, T. M., MOONEY, W. D. & WINDLEY, B. F. 2009. Accretionary orogens through Earth history. In *Earth Accretionary Systems in Space and Time* (eds P. A. Cawood & A. Kröner), pp. 1–36. Geological Society of London, Special Publication no. 318.

CHEN, B. & JAHN, B. M. 2002. Geochemical and isotopic studies of the sedimentary and granitic rocks of the Altai orogen of northwest China and their tectonic implications. *Geological Magazine* **139**, 1–13.

CLOOS, M. 1993. Lithosphere buoyancy and collisional orogenesis: subduction of oceanic plateaus, continental margins, island arcs, spreading ridges, and seamounts. *Geological Society of America Bulletin* **105**, 715–37.

COLEMAN, R. G. 1977. *Ophiolites*. New York: Springer-Verlag, 220 pp.

DEFANT, M. J. & DRUMMOND, M. S. 1993. Mount St. Helens: potential example of the partial melting of the subducted lithosphere in a volcanic arc. *Geology* **21**, 547–50.

DEFANT, M. J., JACKSON, T. E. & DRUMMOND, M. S. 1992. The geochemistry of young volcanism throughout western Panama and southeastern Costa Rica: an overview. *Journal of Geological Society, London* **149**, 569–79.

DICK, H. J. B. & BULLEN, T. 1984. Chromian spinel as a petrogenetic indicator in abyssal and alpine-type peridotites and spatially associated lavas. *Contributions to Mineralogy and Petrology* **86**, 54–76.

DILEK, Y. & FLOWER, M. F. J. 2003. Arc-trench roll-back and forearc accretion (2): a model template for ophiolites in Albania, Cyprus, and Oman. In *Ophiolites in Earth History* (eds Y. Dilek & R. T. Robinson), pp. 43–68. Geological Society of London, Special Publication no. 218.

DILEK, Y. & FURNES, H. 2011. Ophiolite genesis and global tectonics: geochemical and tectonic fingerprinting of ancient oceanic lithosphere. *Geological Society of America Bulletin* **123**, 387–411.

FANG, A. M., WANG, S. G., ZHANG, J. M., ZANG, M., FANG, J. H. & HU, J. M. 2015. The U–Pb ages of the zircons from the gabbro in the Kalamaili ophiolite, North Xinjiang and its tectonic significances. *Chinese Journal of Geology* **50**, 140–54 (in Chinese with English abstract).

FRANZ, L. & WIRTH, R. 2000. Spinel inclusions in olivine of peridotite xenoliths from TUBAF seamount (Bismark Archipelago/Papua New Guinea): evidence for the thermal and tectonic evolution of the oceanic lithosphere. *Contributions to Mineralogy and Petrology* **140**, 283–95.

FURNES, H., PEDERSEN, R. B. & HERTOGEN, J. 1991. Magma development of the Leka ophiolite complex, central Norwegian Caledonides. *Lithos* **27**, 259–77.

https://doi.org/10.1017/S0016756816000042 Published online by Cambridge University Press

GENG, J. Z., LI, H. K., ZHANG, J. & ZHANG, Y. Q. 2011. Zircon Hf isotope analysis by means of LA-MC-ICP-MS. *Geological Bulletin of China* **30**, 1508–13 (in Chinese with English abstract).

HASTIE, A. R., MITCHELL, S. F., KERR, A. C., MINIFIE, M. J. & MILLAR, I. L. 2011. Geochemistry of rare high-Nb basalt lavas: are they derived from a mantle wedge metasomatised by slab melts? *Geochimica et Cosmochimica Acta* **75**, 5049–72.

HELLEBRAND, E., SNOW, J. E., DICK, H. J. B. & HOFMANN, A. W. 2001. Coupled major and trace elements as indicators of the extent of melting in the mid-ocean-ridge peridotites. *Nature* **410**, 677–81.

HELLEBRAND, E., SNOW, J. E. & MÜHE, R. 2002. Mantle melting beneath Gakkel Ridge (Arctic Ocean): abyssal peridotite spinel compositions. *Chemical Geology* **182**, 227–35.

HOFMANN, A. W. & JOCHUM, K.P. 1996. Source characteristics derived from very incompatible trace elements in Mauna Loa and Mauna Kea basalts, Hawaii Scientific Drilling Project. *Journal of Geophysical Research: Solid Earth (1978–2012)* **101**, 11831–9.

HOLLINGS, P. & KERRICH, R. 2000. An Archean arc basalt-Nb-enriched basalt-adakite association: the 2.7 Ga confederation assemblage of the Birch-Uchi greenstone belt, Superior Province. *Contributions to Mineralogy and Petrology* **139**, 208–26.

HUANG, G. NIU, G. Z., WANG, X. L., GUO, J. & YU, F. 2012. Formation and emplacement age of Karamaili ophiolite: LA-ICP-MS zircon U–Pb age evidence from the diabase and tuff in eastern Junggar, Xinjiang. *Geological Bulletin of China* **31**, 1267–78 (in Chinese with English abstract).

HU, C. B., LIAO, Q. A., FAN, G. M., CHEN, S., WU, W. W., TIAN, J. & WANG, F. M. 2014. Discovery of MOR-type ophiolites from the Dishuiquan region, eastern Junggar (in Chinese). *Chinese Science Bulletin (Chinese Version)* **59**, 2213–22.

JAHN, B. M., WU, F.Y. & CHEN, B. 2000. Granitoids of the Central Asian Orogenic Belt and continental growth in the Phanerozoic. *Transactions of the Royal Society of Edinburgh: Earth Sciences* **91**, 181–93.

JAN, M. Q. & WINDLEY, B. F. 1990. Chromian spinel–silicate chemistry in ultramafic rocks of the Jijal Complex, northwest Pakistan. *Journal of Petrology* **31**, 67–71.

JIAN, P., LIU, D. Y., ZHANG, Q., ZHANG, F. Q., SHI, Y. R., SHI, G. H., ZHANG, L. Q. & TAO, H. 2003. SHRIMP dating of ophiolite and leucogranitic rocks within ophiolite. *Earth Science Frontier* **10**, 439–56 (in Chinese with English abstract).

KAMENETSKY, V. S., CRAWFORD, A. J. & MEFFRE, S. 2001. Factors controlling chemistry of magmatic spinel: an empirical study of associated olivine, Cr-spinel and melt inclusions from primitive rocks. *Journal of Petrology* **42**, 655–71.

KEPPLER, H. 1996. Constraints from partitioning experiments on the composition of subduction-zone fluids. *Nature* **380**, 237–40.

LAGABRIELLE, Y., GUIVEL, C., MAURY, R., BOURGOIS, J., FOURCADE, S. & MARTIN, H. 2000. Magmatic-tectonic effects of high thermal regime at the site of active ridge subduction: the Chile triple junction model. *Tectonophysics* **326**, 255–68.

LI, X. H., LI, W. X., LI, Q. L., WANG, X. C., LIU, Y. & YANG, Y. H. 2010*a*. Petrogenesis and tectonic significance of the 850 Ma Gangbian alkaline complex in South China: evidence from in-situ zircon U–Pb and Hf–O isotopes and whole-rock geochemistry. *Lithos* **114**, 1–15.

LI, X. H., LIU, D. Y., SUN, M., LI, W. X., LIANG, X. R. & LIU, Y. 2004. Precise Sm–Nd and U–Pb isotopic dating of the super-giant Shizhuyuan polymetallic deposit and its host granite, SE China. *Geological Magazine* **141**, 225–31.

LI, X. H., LONG, W. G., LI, Q. L., LIU, Y., ZHENG, Y. F., YANG, Y. H., CHAMBERLAIN, K. R., WAN, D. F., GUO, C. H., WANG, X. C. & TAO, H. 2010*b*. Penglai zircon megacryst: a potential new working reference for microbeam analysis of Hf–O isotopes and U–Pb age. *Geostandards and Geoanalytical Research* **34**, 117–34.

LI, X. H., TANG, G. Q., GONG, B., YANG, Y. H., HOU, K. J., HU, Z. C., LI, Q. L., LIU, Y. & LI, W. X. 2013. Qinghu zircon: a working reference for microbeam analysis of U–Pb age and Hf and O isotopes. *Chinese Science Bulletin* **58**, 4647–54.

LISTER, G. & FORSTER, M. 2009. Tectonic mode switches and the nature of orogenesis. *Lithos* **113**, 274–91.

LIU, Y. S., HU, Z. C., ZONG, K. Q., GAO, C. G., GAO, S., XU, J. & CHEN, H. H. 2010. Reappraisement and refinement of zircon U–Pb isotope and trace element analyses by LA-ICP-MS. *Chinese Science Bulletin* **55**, 1535–46.

LUDWIG, K. R. 2003. *User's Manual for Isoplot 3.00: A Geochronological Toolkit for Microsoft Excel*. Berkeley Geochronology Center Special Publication 4, 73 pp.

LUO, J., XIAO, W. J., WAKABAYASHI, J., HAN, C. M., ZHANG, J. E., WAN, B., AO, S. J., ZHANG, Z. Y., TIAN, Z. H., SONG, D. F. & CHEN, Y. C. 2015. The Zhaheba ophiolite complex in Eastern Junggar (NW China): long lived supra-subduction zone ocean crust formation and its implications for the tectonic evolution in southern Altaids. *Gondwana Research*, published online 6 May 2015. doi: 10.1016/j.gr.2015.04.004.

MIYASHIRO, A. 1974. Volcanic rock series in island arcs and active continental margins. *American Journal of Science* **274**, 32–355.

MONNIER, C., GIRARDEAU, J., MAURY, R. & COTTEN, J. 1995. Back-arc basin origin for the East Sulawesi ophiolite (eastern Indonesia). *Geology* **23**, 851–4.

NICOLAS, A. 1989. *Structure of Ophiolites and Dynamics of Oceanic Lithosphere*. Dordrecht, the Netherlands: Kluwer Academic Publishers, 367 pp.

NIU, Y. L. 1997. Mantle melting and melt extraction processes beneath ocean ridges: evidence from abyssal peridotites. *Journal of Petrology* **38**, 1047–74.

NIU, H. C., SHAN, Q., YU, X. Y., ZHANG, B., LUO, Y. & YANG, W. B. 2009*a*. Geochemistry of Nb-enriched basalt and its significance in Zaheba ophiolite mélange. *Acta Petrologica Sinica* **25**, 916–24 (in Chinese with English abstract).

NIU, H. C., SHAN, Q., ZHANG, B., LUO, Y., YANG, W. B. & YU, X. Y. 2009*b*. Discovery of garnet amphibolite in Zaheba ophiolitic mélange, eastern Junggar, NW China. *Acta Petrologica Sinica* **25**, 1484–91 (in Chinese with English abstract).

NIU, H. C., SHAN, Q., ZHANG, H. Y. & YU, X. Y. 2007. $^{40}Ar/^{39}Ar$ geochronology of the ultrahigh-pressure metamorphic quartz magnesitite in Zaheba, eastern Junggar, Xinjiang. *Acta Petrologica Sinica* **23**, 1627–34 (in Chinese with English abstract).

NIU, Y. L., GILMORE, T., MACKIE, S., GREIG, A. & BACH, W. 2002. Mineral chemistry, whole-rock compositions, and petrogenesis of Leg 176 gabbros: data and discussion. In *Proceedings of the Ocean Drilling Program, Scientific Results, vol. 176* (eds J. H. Natland, H. J. B. Dick, D. J. Miller & R. P. Von Herzen), pp. 1–60. College Station, Texas.

https://doi.org/10.1017/S0016756816000042 Published online by Cambridge University Press

NIU, H. C., ZHANG, H. Y., SHAN, Q. & YU, X. Y. 2008. Discovery of the super-silicic, super-titanic garnets in garnet-pyroxenite in Zaheba ophiolite and its geological significance. *Chinese Science Bulletin* **14**, 2186–91.

OH, C. W., RAJESH, V. J., SEO, J., CHOI, S. J. & LEE, J. H. 2010. Spinel compositions and tectonic relevance of the Bibong ultramafic bodies in the Hongseong collision belt, South Korea. *Lithos* **117**, 198–208.

OTA, T., UTSUNOMIYA, A. & UCHIO, Y. 2007. Geology of the Gorny Altai subduction-accretion complex, southern Siberia: tectonic evolution of an Ediacaran-Cambrian intra-oceanic arc-trench system. *Journal of Asian Earth Sciences* **30**, 666–95.

PEARCE, J. A. 2008. Geochemical fingerprinting of oceanic basalts with applications to ophiolite classification and the search for Archean oceanic crust. *Lithos* **100**, 14–48.

PEARCE, J. A. 2014. Immobile element fingerprinting of ophiolites. *Elements* **10**, 101–8.

POLAT, A. & KERRICH, R. 2001. Magnesian andesites, Nb-enriched basalt-andesites, and adakites from late-Archean 2.7 Ga Wawa greenstone belts, Superior Province, Canada: implications for late Archean subduction zone petrogenetic processes. *Contribution to Mineralogy and Petrology* **141**, 36–52.

SACCANI, E., ALLAHYARI, K., BECCALUVA, L. & BIANCHINI, G. 2013. Geochemistry and petrology of the Kermanshah ophiolite (Iran): implication for the interaction between passive rifting, oceanic accretion, and OIB-type components in the Southern Neo-Tethys Ocean. *Gondwana Research* **24**, 392–411.

SAJONA, F. G., MAURY, R. G., BELLON, H., COTTON, J. & DEFANT, M. 1996. High field strength element enrichment of Pliocene–Pleistocene island arc basalts, Zamboanga Peninsula, Western Mindanao (Philippines). *Journal of Petrology* **37**, 693–726.

SANTOSH, M., SHAJI, E., TSUNOGAE, T., RAM MOHAN, M., SATYANARAYANAN, M. & HORIE, S. K. 2013. Suprasubduction zone ophiolite from Agali hill: petrology, zircon SHRIMP U–Pb geochronology, geochemistry and implications for Neoarchean plate tectonics in southern India. *Precambrian Research* **231**, 301–24.

SANTOSH, M., XIAO, W. J., TSUNOGAE, T., CHETTY, T. R. K. & YELLAPPA, T. 2012. The Neoproterozoic subduction complex in southern India: SIMS zircon U–Pb ages and implications for Gondwana assembly. *Precambrian Research* **192–195**, 190–208.

SAUNDERS, A. D., NORRY, M. J. & TARNEY, J. 1991. Fluid influence on the trace element compositions of subduction zone magmas. *Philosophical Transactions of the Royal Society of London* **335**, 377–92.

SCHIANO, P., CLOCCHIATTI, R., SHIMUZU, N., MAURY, R. C., JOCHUM, K. P. & HOFMANN, A. W. 1995. Hydrous silica-rich melts in the sub-arc mantle and their relationship with erupted arc lavas. *Nature* **377**, 595–600.

ŞENGÖR, A. M. C., NATALIN, B. A. & BURTMAN, V. S. 1993. Evolution of the Altaid tectonic collage and Palaeozoic crustal growth in Eurasia. *Nature* **364**, 299–307.

SHEN, X. M., ZHANG, H. X., WANG, Q., MA, L. & YANG, Y. H. 2014. Early Silurian (~440 Ma) adakitic, andesitic and Nb-enriched basaltic lavas in the southern Altay Range, Northern Xinjiang (western China): slab melting and implications for crustal growth in the Central Asian Orogenic Belt. *Lithos* **206–207**, 234–51.

STERN, R. J. 2002. Subduction zones. *Reviews of Geophysics* **40**, 3-1–3-38.

SUN, M., LONG, X. P., CAI, K. D., JIANG, Y. D., WANG, B. Y., YUAN, C., ZHAO, G. C., XIAO, W. J. & WU, F. Y. 2009. Early Paleozoic ridge subduction in the Chinese Altai: insight from the abrupt change in zircon Hf isotopic compositions. *Science in China Series D – Earth Sciences* **52**, 1345–58.

SUN, S. S. & MCDONOUGH, W. F. 1989. Chemical and isotopic systematics of oceanic basalt: implication for mantle composition and processes. In *Magmatism in the Ocean Basin* (eds A. D. Saunders & M. J. Norry), pp. 528–48. Geological Society of London, Special Publication no. 42.

SUN, M., YUAN, C., XIAO, W., LONG, X., XIA, X., ZHAO, G., LIN, S., WU, F. & KRONER, A. 2008. Zircon U–Pb and Hf isotopic study of gneissic rocks from the Chinese Altai: progressive accretionary history in the early to middle Palaeozoic. *Chemical Geology* **247**, 352–83.

TONG, Y., WANG, T., HONG, D. W., DAI, Y. J., HAN, B. F. & LIU, X. M. 2007. Ages and origin of the early Devonian granites from the north part of Chinese Altai Mountains and its tectonic implications. *Acta Petrologica Sinica* **23**, 1933–44 (in Chinese with English abstract).

VALLEY, J. W., KINNY, P. D., SCHULZE, D. J. & SPICUZZA, M. J. 1998. Zircon megacrysts from kimberlite: oxygen isotope variability among mantle melts. *Contributions to Mineralogy and Petrology* **133**, 1–11.

WANG, T., HONG, D. W., JAHN, B. M., TONG, Y., WANG, Y. B., HAN, B. F. & WANG, X. X. 2006. Timing, petrogenesis, and setting of Paleozoic synorogenic intrusions from the Altai Mountains, northwest China: implications for the tectonic evolution of an accretionary orogen. *Journal of Geology* **114**, 735–51.

WANG, T., JAHN, B. M., KOVACH, V. P., TONG, Y., HONG, D. W. & HAN, B. F. 2009. Nd–Sr isotopic mapping of the Chinese Altai and implications for continental growth in the Central Asian Orogenic Belt. *Lithos* **110**, 359–72.

WILHEM, C., WINDLEY, B. F. & STAMPFLI, G. M. 2012. The Altaids of Central Asia: a tectonic and evolutionary innovative review. *Earth-Science Reviews* **113**, 303–41.

WINCHESTER, J. A. & FLOYD, P. A. 1977. Geochemical discrimination of different magma series and their differentiation products using immobile elements. *Chemical Geology* **20**, 325–43.

WINDLEY, B. F., KRONER, A., GUO, J., QU, G., LI, Y. & ZHANG, Z. C. 2002. Neoproterozoic to Paleozoic geology of the Altai orogen, NW China: new zircon age data and tectonic evolution. *Journal of Geology* **110**, 719–39.

WU, B., HE, G. Q., WU, T. R., LI, H. J. & LUO, H. L. 2006. Discovery of the Buergen ophiolitic mélange belt in Xinjiang and its tectonic significance. *Geology in China* **33**, 476–86 (in Chinese with English abstract).

XIAO, W. J., HAN, C. M., LIU, W., WAN, B., ZHANG, J. E., AO, S. J., ZHANG, Z. Y., SONG, D. F., TIAN, Z. H. & LUO, J. 2014. How many sutures in the southern Central Asian Orogenic Belt: insights from East Xinjiang–West Gansu (NW China)? *Geoscience Frontiers* **5**, 525–36.

XIAO, W. J., HAN, C. M., SUN, M., LIN, S. F., CHEN, H. L., LI, Z. L., LI, J. L. & SUN, S. 2008. Middle Cambrian to Permian subduction-related accretionary orogenesis of North Xinjiang, NW China: implications for the tectonic evolution of Central Asia. *Journal of Asian Earth Sciences* **32**, 102–17.

XIAO, W. J., WINDLEY, B. F., ALLEN, M. B. & HAN, C. M. 2013. Paleozoic multiple accretionary and collisional tectonics of the Chinese Tianshan orogenic collage. *Gondwana Research* **23**, 1316–41.

XIAO, W. J., WINDLEY, B. F., BADARCH, G., SUN, S., LI, J. L., QIN, K. Z. & WANG, Z. H. 2004. Palaeozoic accretionary and convergent tectonics of the southern Altaids: implications for the lateral growth of Central Asia. *Journal of Geological Society, London* **161**, 339–42.

https://doi.org/10.1017/S0016756816000042 Published online by Cambridge University Press

XIAO, W. J., WINDLEY, B. F., HUANG, B. C., HAN, C. M., YUAN, C., CHEN, H. L., SUN, M., SUN, S. & LI, J.L. 2009*a*. End-Permian to middle Triassic termination of the accretionary processes of the southern Altaids: implications for the geodynamic evolution, Phanerozoic continental growth, and metallogeny of Central Asia. *International Journal of Earth Sciences* **98**, 1189–217.

XIAO, W. J., WINDLEY, B. F., YUAN, C., SUN, M., HAN, C. M., LIN, S. F., CHEN, H. L., YAN, Q. R., LIU, D. Y., QIN, K. Z. & SUN, S. 2009*b*. Paleozoic multiple subduction-accretion processes of the southern Altaids. *American Journal of Sciences* **309**, 221–70.

XINJIANG, BGMR. 1993. *Regional Geology of the Xinjiang Uygur Autonomous Region*. Beijing: Geological Publishing House, pp. 2–145 (in Chinese).

YE, X. T., ZHANG, C. L., ZOU, H. B., ZHOU, G., YAO, C. Y. & DONG, Y. G. 2015. Devonian Alaskan-type ultramafic-mafic intrusions and silicic igneous rocks along the southern Altai Orogen: implications on the Phanerozoic continental growth of the Altai Orogen of the Central Asian Orogenic Belt. *Journal of Asian Earth Sciences* **113**, 75–89.

YELLAPPA, T., SANTOSH, M., CHETTY, T. R. K., KWON, S., PARK, C., NAGESH, P., MOHANTY, D. P. & VENKATASIVAPPA, V. 2012. A Neoarchean dismembered ophiolite complex from southern India: geochemical and geochronological constraints on its suprasubduction origin. *Gondwana Research* **21**, 246–65.

YUAN, C., SUN, M., XIAO, W., LI, X., CHEN, H., LIN, S., XIA, X. & LONG, X. 2007. Accretionary orogenesis of the Chinese Altai: insights from Paleozoic granitoids. *Chemical Geology* **242**, 22–39.

YUAN, C., XIAO, W. J., CHEN, H. L., LI, J. L. & SUN, M. 2006. Zhaheba potassic basalt, eastern Junggar (NW China): geochemical characteristics and tectonic implications. *Acta Geologica Sinica* **80**, 254–63 (in Chinese with English abstract).

ZHANG, H. X., NIU, H. C., TERADA, K., YU, X. Y., SATO, H. & ITO, J. 2003. Zircon SHRIMP U–Pb dating on plagiogranite from Kuerti ophiolite in Altay, North Xinjiang. *Chinese Science Bulletin* **48**, 2231–5.

ZHANG, C. L., SANTOSH, M., ZOU, H. B., LI, H. K. & HUANG, W. C. 2013. The Fuchuan ophiolite in Jiangnan Orogen: geochemistry, zircon U–Pb geochronology, Hf isotope and implications for the Neoproterozoic assembly of South China. *Lithos* **179**, 263–74.

ZHANG, C. L., SANTOSH, M., ZOU, H. B., XU, Y. G., ZHOU, G., DONG, Y. G., DING, R. F. & WANG, H.Y. 2012. Revisiting the "Irtish tectonic belt": implications for the Paleozoic tectonic evolution of the Altai orogen. *Journal of Asian Earth Sciences* **52**, 117–33.

ZHANG, H. X., SHEN, X. M., MA, L., NIU, H. C. & YU, X. Y. 2008. Geochronology of Fuyun adakite, northern Xinjiang and its constraint to the initiation of the Paleo-Asian ocean subduction. *Acta Petrologica Sinica* **24**, 1054–58 (in Chinese with English abstract).

ZINDLER, A. & HART, S. R. 1986. Chemical geodynamics. *Annual Review of Earth and Planetary Sciences* **14**, 493–571.

https://doi.org/10.1017/S0016756816000042 Published online by Cambridge University Press